

Interactive wave-structure impacts in aerated water

Numerical modeling of interactive rigid body motion in aerated water wave impacts

M.M. Bockstael

Delft University of Technology

Thesis for the degree of MSc in Marine Technology in the specialization of ship hydromechanics

Interactive wave-structure impacts in aerated water

**Numerical modeling of interactive rigid body
motion in aerated water wave impacts**

by

M.M. Bockstael

4385179

Thesis committee:

Daily supervisor: Ir. M. van der Eijk
Chair: Dr. Ir. P.R. Wellens
Staff member: Dr. Ir. M.J.B.M. Pourquie
Staff member: Dr. Ir. G.H. Keetels

Institution: Delft University of Technology
Place: Faculty of Mechanical, Maritime and Materials Engineering, Delft
Project Duration: June, 2020 - April, 2021
Author contact: mbockstael@protonmail.com

Cover Image: Lighthouse by Lena Khрупina - Pexels.com

Abstract

Marine structures can sustain damage due to violent wave impacts that are characterized by complex dynamics involving both water and air. Methods that predict impacts loads for structural design often assume the water as incompressible. These predictions can be inaccurate during impacts where air is entrained in water, as that greatly increases its compressibility. Initial impact forces may decrease due to a cushioning effect. However, the total severity of the impact may increase due to temporal spreading and oscillations of impact pressure.

Previous research on aerated water impacts covers breaking waves against fixed structures, flat water slamming or green water events, but not the interactive motion of rigid marine structures in free surface waves. This work aims to evaluate the effect of aerated water impacts on the dynamics of floating rigid bodies in irregular waves.

As a part of this work, a state-of-the-art numerical simulation method for aerated water impacts is extended with a monolithic coupling for rigid body motion. Additionally, boundary conditions for wave generation were implemented for a validation of the method during breaking wave impact. Results of the verification of both extensions compare well to other literature.

It was found for cylinder slamming in aerated water with entry velocity Mach numbers below 0.1 that the depth of penetration after impact is affected most by the reduced density of the water-air mixture, not by its increased compressibility. However, the sustained peak impact force was 19% lower due to compressibility in aerated water with a void fraction of 0.05 during slamming with an entry Mach number of 0.074.

During a flip-through wave impact, a 35% reduction of maximum additional effort on a wall was found for a void fraction of 0.05, while the reduction of peak pressure was less than 10%. Flow velocities during impact easily exceeded Mach 0.3, which is the limiting condition for incompressibility. The reduced speed of sound due to a void fraction of 0.05 can double the intensity of reflected pressures in corners of impact-surrounding closed domains. High pressure gradients were found due to the slower propagation of pressure waves, which were strong enough to lift a concrete block.

It can be concluded from this thesis that the compressibility effects of aeration on penetration depth after cylinder slamming can be neglected for entry Mach numbers below 0.1. For further research, it is recommended that this numerical method is used for a range of experiments with various geometries and higher impact velocities. This could provide more insight into situations where aerated water could have important design implications.

Preface

What better to do during a global pandemic than spending hours and hours on coding while trying to understand complex fluid simulation methods? I could think of a few things. All jokes aside, this graduation project has taught me a lot about the fascinating world of numerical fluid simulation, but also about myself. I have enjoyed my study career a lot and it feels rewarding to bring it all together now.

I have not done this alone and would like to give my thanks here to the people that were involved with this project. First and most of all, I would like to thank my daily supervisor Martin van der Eijk for his availability for help and questions during this project. Martin has extended the boundaries of daily supervision to the weekends and nights as well, and I realize that is a luxury not all graduation students have. Without his help, I could not have gotten to the point I am now.

I would also like to thank the chair of the graduation committee, Peter Wellens, for taking me in as a graduation student. His constructive and motivating criticism during progress meetings and pushes in the right direction when most needed are greatly appreciated.

I thank the full thesis committee in advance for their time during the reading of this thesis and during the coming defense.

Last but not least, I want to thank my mom and dad, brother and sister, girlfriend and mates for making all these years so enjoyable.

*M.M. Bockstael
Rotterdam, April 2021*

Contents

Abstract	i
Preface	ii
Nomenclature	vi
List of Figures	viii
List of Tables	x
1 Introduction	1
1.1 Background	2
1.1.1 Societal relevance	2
1.1.2 Physical relevance	2
1.1.3 Theoretical model	3
1.1.4 Problem statement	4
1.2 Research approach	4
1.2.1 Gap analysis	4
1.2.2 Numerical method	5
1.2.3 Objective and novelty	5
1.3 Outline	6
2 Numerical method	7
2.1 Introduction	7
2.1.1 Description of the original method	7
2.1.2 New state of the method	8
2.2 Governing equations	9
2.2.1 Continuity equation	9
2.3 Solution method	10
2.3.1 Sequence of variable calculation	10
2.3.2 Density of water and air	11
2.3.3 Intermediate velocity	11
2.3.4 Poisson equation for the pressure	12
2.3.5 New velocity and CFL controller	13
2.4 Coupling with body motion	13
2.4.1 Added-mass effect	14
2.4.2 Strong coupling	14
2.4.3 Restricted direction	15
3 Wave generation	16
3.1 Wave theory	16
3.1.1 Linear potential wave	16
3.1.2 Rienecker-Fenton wave	17
3.1.3 Third-order Stokes wave	18
3.2 Inflow conditions	18
3.2.1 Free surface elevation	19
3.2.2 Inflow velocities	19
3.3 Single periodic wave	20
3.3.1 Periodic boundary conditions	20
3.3.2 Initial conditions and air velocity	20
3.4 Conclusion	21
4 Verification and validation	22
4.1 Buoyant cylinder water entry	22
4.1.1 Numerical setup	23
4.1.2 Validation results	23

4.1.3	Influence of aeration	24
4.1.4	Conclusion	26
4.1.5	Discussion	27
4.2	Regular wave propagation	28
4.2.1	Numerical setup	28
4.2.2	Free surface and velocity profile	28
4.2.3	Wave height dissipation	29
4.2.4	Conclusion	30
4.3	Wave impact on a fixed wall	30
4.3.1	Numerical setup	30
4.3.2	Impact dynamics	31
4.3.3	Pressure waves	34
4.3.4	Flow velocities	35
4.3.5	Conclusion	35
4.4	Conclusion	35
5	Wave impact on a pendulum	37
5.1	Monolithic coupling for pendulum motion	37
5.2	Numerical setup	39
5.2.1	Free vibration test	39
5.2.2	The numerical wave tank	39
5.3	Irregular focused wave	41
5.3.1	Fourier analysis for wave components	41
5.3.2	Reflection at closed boundary	41
5.4	Impact on pendulum	42
5.5	Conclusion	43
5.6	Discussion	44
5.6.1	Swing radius of the pendulum	44
5.6.2	Total volume of the pendulum bob	45
6	Conclusion	46
7	Discussion	48
7.1	Range of applicability	48
7.2	Recommendations for further research	49
7.3	Comments on method implementations	49
	Bibliography	51
A	Literature review	54
A.1	Aerated water impacts	54
A.1.1	Wave impact	54
A.1.2	Slamming	55
A.1.3	Green water	55
A.2	Fluid-structure interaction in two-phase flow methods	56
A.3	Wave generation in two-phase flow methods	57
A.4	Conclusion	57
B	VoF fractions and labelling	59
B.1	Interface modeling	59
B.1.1	Reconstruction	59
B.1.2	Cell apertures	59
B.2	Interface displacement	60
B.2.1	Fluid-fluid interface	60
B.2.2	Fluid-solid interface	60
B.2.3	Labelling of internal body cells	61
B.2.4	Virtual cell merging	61
C	Material derivative of the density	62
D	Additions to the numerical method	64
D.1	Arbitrary fraction field initialisation	64

D.2	Stretching grid cells	65
D.2.1	Simple.	65
D.2.2	Detail	65
E	Initial periodic wave comparison	67
F	Focused step wave	68

Nomenclature

Abbreviations

Abbreviation	Definition
DoF	Degrees of Freedom
PLIC	Piecewise Linear Interface Construction
VoF	Volume of Fluid

Symbols

Symbol	Definition	Unit
A	LHS matrix in Poisson equation	
A_f	Body force coupling matrix	
B	Amount of liquid in a cell in Chapter 2	[-]
C	Discrete convection operator in § 2.3.3	
D	Discrete diffusion operator in § 2.3.3	
F	VoF-variable in Chapter 2 and Appendix B	[-]
F	Force in Chapter 4 and Chapter 5	[N m ⁻¹]
F_b	Solid fraction	[-]
F_s	Fluid fraction	[-]
G	Discrete gradient operator in § 2.3.3	
H	Wave height in Chapter 3	[m]
I	Rotational inertia of pendulum in Chapter 5	[kg m ²]
M	Mach number	[-]
M	External moment in Chapter 5	[-]
M_{ce}	Cylinder entry velocity Mach number	[-]
Q_b	Body velocity coupling matrix	
T	Coupling direction matrix	
a	Wave amplitude in § 3.1.3	[m]
c_l, c_w, c_a	Speed of sound pure water, water mixture, pure air	[m s ⁻¹]
c	Group velocity in Chapter 3	[m s ⁻¹]
c	Damping coefficient of pendulum in Chapter 5	[N m s rad ⁻¹]
f	External fluid force term	[m s ⁻²]
f_b	Force on solid body (2D)	[N m ⁻¹]
h	Water depth	[m]
k	Restoring force coefficient of pendulum in Chapter 5	[N m]
k	Wave number in Chapter 3	[rad m ⁻¹]
l	Length	[m]
m	Mass	[kg]
p	Pressure	[Pa]
p_0	Reference or atmospheric pressure	[Pa]
q	RHS vector in Poisson equation	
t	Time	[s]
r	Radius	[m]
u	Fluid bvelocity	[m s ⁻¹]
u_b	Body velocity	[m s ⁻¹]
u_x, u	Horizontal velocity	[m s ⁻¹]
u_z, v	Vertical velocity	[m s ⁻¹]
w	Width	[m]
x	Horizontal coordinate	[m]

Symbol	Definition	Unit
y, z	Vertical coordinate	[m]
Φ	Velocity potential	[m ² s ⁻¹]
Ψ	Stream function	[m ² s ⁻¹]
β	Volume/void fraction	[-]
$\beta \cdot 100\%$	Aeration level	[%]
ϵ	Wave phase difference in Chapter 3	[rad]
ℓ	Length of the pendulum in Chapter 5	[m]
μ	Dynamic viscosity	[kg m ⁻¹ s ⁻¹]
ω	Wave frequency	[rad s ⁻¹]
ρ	Density	[kg/m ³]
ρ_0	A reference density at p_0	[kg/m ³]
ρ_l	Density of pure water	[kg m ⁻³]
ρ_g	Density of pure air in dispersed bubbles	[kg m ⁻³]
ρ_a	Density of pure air above the free surface	[kg m ⁻³]
ρ_w	Density of aerated water mixture	[kg m ⁻³]
ρ^*, ρ^{**}	Auxiliary densities in § 2.3.3	[kg/m ³]
θ	Wave phase in Chapter 3	[rad]
θ	Pendulum deflection angle in Chapter 5	[rad]
ζ, η	Wave elevation	[m]

List of Figures

1.1	Speed of sound as a function of void fraction (Plumerault, 2009).	4
2.1	Schematic depiction of cell labeling, geometry reconstruction and VoF fractions	8
2.2	Sequence of variable calculation	10
3.1	Schematic depiction of inflow conditions for wave motion	19
3.2	Initial horizontal velocity field according to inflow conditions including extrapolated air velocities.	20
4.1	Flat water entry of 2D buoyant cylinder	22
4.2	Free falling buoyant cylinder from $h = 1.00$ m with $m = m_0 + 1$ kg, compared to physical experiment (Russo et al., 2017).	23
4.3	Impact velocities V_{im} recorded during the simulations, compared to physical experiment (Russo et al., 2017).	24
4.4	Penetration through the free surface compared to physical and numerical experiments of Russo et al. (2017) and Facci et al. (2019).	24
4.5	Dimensionless vertical force during impact with aeration $\beta = 0.05$ and reduced density $\rho = 950$ kg m ⁻³ . Right figure zooms in on the missing peak of the left figure. The black circle indicates the sustained impact force.	25
4.6	Maximum force during aerated water impact (F_β) relative to the maximum impact force during reduced density impact (F_ρ) for increasing cylinder entry Mach number M_{ce}	26
4.7	Gage pressure at left bottom corner of the domain during aerated impact with $\beta = 0.05$ and during reduced density impact with $\rho_l = 950$ kg m ⁻³	26
4.8	Penetration depth, impact velocity and force for different solver and domain settings.	27
4.9	Penetration depth and impact force for different cylinder resolutions.	28
4.10	Free surface profile of first two wave lengths (on the left) and the horizontal velocity profile (on the right) in a crest and a trough at the positions indicated by the corresponding colored vertical lines in the left figure. The positioning of horizontal grid lines is equal to the numerical cell spacing.	29
4.11	Free surface profile of Rienecker-Fenton wave over the first 500 m (on the left) and the relative wave height dissipation (on the right).	30
4.12	Visual description of the breaking wave experiment.	31
4.13	Snapshots of free-surface leading up to impact for $t/T=0.27, 0.31, 0.35$ (different times in reference free-surface, but similar $\Delta t/T$).	32
4.14	Additional total effort on the wall per meter depth, relative to quasi-hydrostatic effort $F_0 = 1.15 \cdot 10^6$ N m ⁻¹	33
4.15	Spatio-temporal evolution of $p - p_0$ at the wall for 5.0% aeration.	33
4.16	Spatial distribution of dimensionless pressure on the vertical wall at $t = t(p_{max})$	33
4.17	Dimensionless pressure history at the foot of the structure (lower right corner of the domain) for different aeration levels.	34
4.18	Highest recorded vertical flow Mach numbers at different altitudes and aeration levels.	35
5.1	Schematic overview of the experimental setup (Bos and Wellens, 2021).	38
5.2	Free vibration test in air.	40
5.3	Image of the numerical wave tank used for the case study (approx. 12000 cells).	40
5.4	Experimental measured wave height at the inflow wave gauge.	41
5.5	Wave heights compared to experimental measurements for different domain lengths at the inflow (top), pendulum (middle), and final wave meter (bottom).	42
5.6	Angular deflection over time compared to the experiment.	43
5.7	Change in radius (left) and total volume (right) of the bob compared to their initial values in the free vibration test.	44

E.1 Comparison between wave with and without extrapolating initial air velocities. It shows no observable differences in the fluid velocities. 67

F.1 Snapshots of the steep wave impact on the pendulum. 69

List of Tables

4.1	Simulation parameters for Rienecker-Fenton wave propagation.	28
5.1	Stretched grid parameters for numerical wave tank in case study.	40
F.1	Wave parameters for focused wave in Chapter 5.	68

1

Introduction

Marine structures, such as ships or coastal protection, can sustain damage due to violent wave impacts. Such impacts are extreme free-surface events with complex dynamic characteristics involving both water and air. Recently, it is shown that the effect of air on these kinds of impacts should not always be neglected.

Analytical and numerical models that are used to predict the loads during wave impact often assume the water as incompressible and neglect the air phase. When air is entrained in water, the compressibility of the aerated mixture is greatly increased (Wood, 1946). The entrapment of larger pockets of compressible air can cause pressure oscillations of significant magnitude (van der Eijk and Wellens, 2019). The total severity of an aerated water impact is not necessarily lower, despite an initial cushioning effect (Bullock et al., 2007).

Several physical and numerical studies on aerated water impacts exist that concern breaking waves against fixed structures (Bullock et al., 2007; Bredmose et al., 2009; Plumerault et al., 2012), flat water slamming (Ma et al., 2016; Elhimer et al., 2017; Mai et al., 2019a; Aghaei et al., 2020) or a green water event (van der Eijk, 2018; van der Eijk and Wellens, 2021a). No studies have considered the interactive motion of rigid marine structures. Evaluating the effect of aerated water impacts on the dynamics of freely floating rigid bodies in irregular waves is **the aim of this thesis**.

This study employs the numerical simulation method under the working name EVA, which is designed specifically for the simulation of aerated water impacts. **The main objective of this work** is to extend the method EVA by adding a rigid body motion coupling method. **The secondary objective of this work** is to implement wave-generation methods for the validation of EVA for breaking wave impacts. Extending the state-of-the-art in aerated water impact modeling with interactively moving rigid bodies in irregular waves is **the novelty in this work**.

Following this general introduction, the rest of this chapter further introduces the reader to the problem background in Section 1.1, the research approach of the presented study in Section 1.2 and the outline for the rest of this thesis in Section 1.3.

1.1. Background

To further introduce the reader into the context of aerated water impacts, this section provides a background. First the societal relevance of hydrodynamic impacts is stressed in § 1.1.1. The physical occurrence and relevance of aerated water impacts are briefly introduced in § 1.1.2. Following this, we describe the properties of aerated water according to a theoretical model in § 1.1.3. This section concludes with the problem statement in § 1.1.4.

1.1.1. Societal relevance

As the ocean covers 70% of the Earth's surface, it is no surprise that we use it for many different resources. Take for example the increasing global consumption of fish (FAO, 2020) or the potential of harvesting energy directly from the ocean (Mwasilu and Jung, 2018). From this and more, it can be stated that a large part of today's global society depends heavily on the sea and, consequently, also on coastal and sea-going operations.

The structural design of any vessel or offshore structure is led by the loads it is expected to endure during its lifetime. The goal is to create effective structures that are cost-efficient and safe for the people that operate them. Scientists and marine engineers can provide society with more and better tools for estimating structural loads, thereby increasing longevity and safety of ships.

Large structural loads can be caused by hydrodynamic impacts during extreme free surface events, like wave impacts. For different types of wave impacts, the effect of an air-water mixture should not be neglected (e.g. slamming (Mai et al., 2019a), breaking waves (Mai et al., 2019b) and green water loading (van der Eijk and Wellens, 2021a)). But before design considerations can be made, it is up to marine engineers to provide the tools for realistic hydrodynamic impact load estimation including the effect of air.

1.1.2. Physical relevance

The effect of air on hydrodynamic wave impacts is split in two ways, making a distinction similar to (Plumerault, 2009; van der Eijk, 2018; van der Eijk and Wellens, 2021a). On a larger scale there is the possibility that volumes of air are trapped between wave and impacted structure. On a smaller scale the air can be entrained in the water so that it becomes a dispersed mixture. This last physical process is referred to as aeration.

Aeration and air entrapment are closely related to each other, as air entrapment and the fragmentation of the resulting air pocket can lead to aeration of the water (Ma et al., 2014). Other causes of aeration are biological production, steep capillary waves and white capping (Crawford, 1999). Both (van der Eijk, 2018) and (Plumerault, 2009) give a summary on naturally occurring air bubble rates found in literature, but could make no clear conclusion as findings differ a lot from study to study. These differences are expectedly caused by the complexity of the phenomenon and the measurements (Plumerault, 2009). Although no clear conclusions can be drawn to determine a common or average level of aeration, values over 1% have been reported (Bullock et al., 2001). Additionally, bubbles seem to persist up to several wave periods longer in seawater compared to fresh water (Bullock et al., 2001). This indicates that the study of aerated water impacts is especially relevant for structures that operate on the ocean, where extreme free surface events are also most likely.

Not only are air entrapment and aeration related in origin, but also in their effect on hydrodynamic impacts. Due to the presence of aerated water, a cushioning effect can be observed during impact (Bullock et al., 2007). Entrapped air may cause pressure oscillations with a similar order of magnitude as the impact itself, due to compression waves in the air pocket (van der Eijk and Wellens, 2019). The frequencies of pocket oscillations and speed of pressure waves through aerated water can cause

unexpected forces, like a large seawards turning moment on a vertical wall (Plumerault, 2009). A more extensive overview of studies on aerated water impacts is provided in Section A.1, but first a theoretical model for aerated water is introduced in § 1.1.3.

1.1.3. Theoretical model

This subsection introduces a theoretical model for aerated water, that captures the different fluid dynamics that we are interested in. The following theoretical model for aerated water as a homogeneous dispersed mixture of air bubbles in water is based on the study by Plumerault (2009), which was also used in the work that this thesis builds on (van der Eijk, 2018; van der Eijk and Wellens, 2021a). This assumption states that there is a homogeneous bulk density and compressibility in the mixture. The relations in this model are thus all for a homogeneously dispersed mixture composed of water and air bubbles, where the pressure is assumed continuous through both fluids.

While the density and compressibility are not directly of interest here, the effect they have on pressure dynamics during impacts is. In acoustics, the change in pressure p is related to the change in density ρ by the following isentropic relation (Kundu et al., 2016):

$$\frac{Dp}{Dt} = c^2 \frac{D\rho}{Dt} \quad (1.1)$$

where c is the speed of sound in the fluid. As will be explained in this rest of this subsection according to theoretical relations, the compressible properties of the bubbly mixture make pressure gradients last much longer. The different spatial and temporal distribution of pressure in the mixture can affect the resulting forces on a structure, when compared to an incompressible fluid model.

The amount of air in the bubbly mixture is defined as a volume (or void) fraction β of air in water. The bulk density of the mixture is then a weighted average of the liquid density ρ_l and gas density ρ_g :

$$\rho_w = (1 - \beta)\rho_l + \beta\rho_g \quad (1.2)$$

For commonly observable aeration levels (§ 1.1.2), this means that the bulk density of the mixture is still close to that of pure water.

Central to the assumption of the homogeneous dispersed mixture is the expression for the speed of sound c_{w0} in a bubbly mixture by Wood (1946):

$$\frac{1}{\rho_{w0}c_{w0}^2} = \frac{\beta}{\rho_{g0}c_{g0}^2} + \frac{1 - \beta}{\rho_{l0}c_{l0}^2} \quad (1.3)$$

at a reference pressure p_0 . Using this expression, the speed of sound in a bubbly liquid can be shown to become much lower than the speed of sound in air. This theoretical relationship is valid for bubbles well below resonance size of the pressure wave frequency (Plumerault, 2009), and is confirmed experimentally by Wilson and Roy (2008). See Figure 1.1 by Plumerault (2009) for a visualisation of Eq. (1.3). This relationship shows that compressibility increases greatly, while the density remains quite close to the water density for low aeration levels.

The incompressible flow assumption that is commonly used in estimating hydrodynamic impacts becomes invalid for flow Mach numbers $M > 0.3$ (Kundu et al., 2016). This condition evaluates to flow velocities of approximately $15[m/s]$ in a fluid with an air content of 5%, according to Figure 1.1. Such magnitudes of flow velocities are not unrealistic in wave impact events (van der Eijk, 2018). It should also be noted that the acoustic relation Eq. (1.3) is based on isentropic density and pressure fluctuations, meaning that it is only valid for subsonic flows; where $M < 1$.

It is noted here again that the above model is based on a homogeneous mixture and isentropic

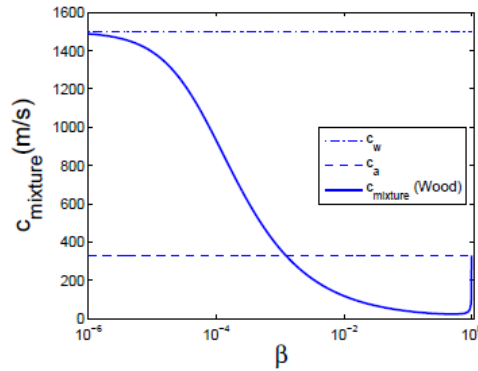


Figure 1.1: Speed of sound as a function of void fraction (Plumerault, 2009).

flow. In reality, it is very unlikely that the dispersion of air bubbles is homogeneous throughout a wave. Also, when air is dissolved in water the assumptions on the acoustics are not valid anymore. Although the presented model does not capture the full complexity of a wave impact with an inhomogeneous distribution of air bubbles that can fragmentate and dissolve, changes in global pressure dynamics and resulting forces can be estimated with it. This model forms the basis of the fluid equations that are used in this numerical study, which are given in Section 2.2.

1.1.4. Problem statement

The reader has now been introduced to the societal and physical relevance of aerated water and a theoretical model to understand the consequences for the pressure dynamics. This subsection serves as a conclusion to this section, and will end with a problem statement.

Hydrodynamic impacts on ships should be understood well to increase the longevity and safety of structures (§ 1.1.1). Especially in seawater, entrained air influences hydrodynamic impacts and could cause unexpected resulting forces or pressure waves (§ 1.1.2). A theoretical model of aerated water as a homogeneous mixture of air bubbles in water indicates compressibility much higher than that of pure water (§ 1.1.3). This leads to the following **problem statement**:

The assumption of incompressible flow during the analysis of hydrodynamic impacts is shown to be invalid in commonly occurring impacts at sea. To predict impact loads more accurately, aerated water needs to be considered in the different types of wave impacts that marine structures have to endure.

1.2. Research approach

This section introduces the reader to the research approach taken in this thesis. First, the current state-of-the-art found during the literature review is summarized in § 1.2.1, which leads to the aim of this work. Second, the numerical method that will be used during this work is introduced in § 1.2.2. Finally, we conclude this section by stating the objectives and novelty of this work in § 1.2.3.

1.2.1. Gap analysis

This subsection serves as a short summary of the conclusions of the literature review in Appendix A. Both physical and numerical studies indicate that aerated water impacts can be characterized by less localised and lower peak loads. However, due to wider temporal spreading the total impulse might be just as severe. Strong pressure gradients and resonant behaviour may occur due to the reduced speed of sound in aerated water. Numerical methods capable of modeling these phenomena have been employed for studying breaking wave impacts, wave slamming or green water loading. None of

these studies have considered rigid body dynamics of floating objects in free surface waves. This leads to the following **aim of this thesis**:

To evaluate the effect of aerated water impacts on rigid body dynamics of freely floating objects in free surface waves.

1.2.2. Numerical method

This thesis builds on recent developments to a new method for aerated water modeling, that currently goes under the working name EVA. It will be used to evaluate the effect of aeration in interactive wave-structure impacts on rigid bodies. It has been introduced and used in (van der Eijk, 2018) to evaluate the effect of aeration on green water loading events, as was discussed at the end of § A.1.3. Currently it is under development by van der Eijk and Wellens (2021a,b) in unpublished work. It is a finite-volume Navier-Stokes solver that models aerated water as a homogeneous mixture of water and air (§ 1.1.3), similar to (Bredmose et al., 2009; Plumerault et al., 2012; Aghaei et al., 2020). A description of the numerical method is in Chapter 2.

EVA originated as an extension to ComFLOW, which is described thoroughly in (Fekken, 2004; Kleefsman, 2005; Wemmenhove, 2008). ComFLOW is verified by multiple authors and well-validated through physical experiments. Its strength lies in the accurate and stable simulation of highly distorted free surface configurations after wave impacts and in the accurate representation of impact pressures (Wellens, 2012). The design goals of EVA are similar, but extended to include the modeling of aerated water.

There are several other numerical methods that have the capability to model the effects of air (both entrapment and entrained air), but the diffusion of the interface between water and air is not always kept below the resolution of one grid cell. While some impact dynamics can still be predicted quite well, the free surface and any solid surfaces are not represented accurately. The importance of this for the fluid-fluid interface is mentioned in § A.1.1, and also for the fluid-solid interface in Section A.2. In the development of EVA, much attention is paid to keeping both these interfaces sharp by using surface reconstruction, cell labeling and cut-cells.

1.2.3. Objective and novelty

From the previous section it is concluded that the numerical method EVA is promising for the accurate simulation of aerated water impacts and highly distorted free surfaces. Considering that it has already been validated for an aerated dam break impact (van der Eijk, 2018; van der Eijk and Wellens, 2021a), this work will extend it further for the aim of this work. This leads to the **main objective of this graduation project**:

To further extend, verify and validate the numerical method EVA for aerated water impacts by adding a coupling method for rigid body-fluid interaction.

Since this method has been verified and validated using experiments without wave motion, no wave-generating boundary conditions had yet been implemented. For validation and use in physical aerated wave impact events, such as the experiments by (Bullock et al., 2007), these boundary conditions are necessary. In Section A.3 it was found that wave-generating boundary conditions in two-phase flow method often neglect the velocities of air above the free surface. This leads to the **secondary objective of this graduation project**:

To further extend, verify and validate the numerical method EVA for aerated water impacts by implementing wave-generating boundary conditions with specific attention to the air above the free-surface.

Achieving these objectives will help work towards the aim of this thesis as posed in § 1.2.1, and also to extend the state-of-the-art in aerated water impact modeling. To the knowledge of the author, no studies have been reported that evaluate rigid body-fluid interaction in two-phase flow including aerated water (Section A.2). Numerical modeling and evaluation of aerated water impact on interactively moving rigid bodies in irregular waves is **the novelty in this work**.

1.3. Outline

The further contents of this thesis are outlined here. First the internal flow model of the numerical method is described in Chapter 2, where the new rigid body-fluid coupling is also introduced. The external boundary conditions for wave-generation are described in Chapter 3, where wave inflow conditions for two-phase flow and periodic waves are introduced. Results of numerical experiments for verification and validation are presented in Chapter 4.

In Chapter 5 an additional experiment is presented with the simulation of steep irregular wave impact on a pendulum. This is a separate chapter, because we specifically discuss extra implementations of irregular wave generation from Fourier analysis and extend the monolithic coupling for pendulum motion.

Conclusions with regard to the aim and objectives of this thesis are drawn in Chapter 6. This is followed by a discussion in Chapter 7, where the range of applicability, recommendations for further research and the implementation process are discussed.

The appendices contain the literature review in Appendix A. Furthermore, they contain a description of the VoF-method and cell labelling in Appendix B and the derivation of the continuity equation for the aggregated fluid in Appendix C. An overview of the additions to the numerical method is given in Appendix D. The rest of the appendices contain other figures and data.

2

Numerical method

This chapter describes the numerical method (EVA) that was introduced with the research approach in Section 1.2. Specifically, it concerns the internal flow in the domain. The external conditions at the boundaries are not considered here, but included in Chapter 3.

The reader is first referred to the introduction of the method in Section 2.1. Following this introduction, the governing equations for the internal fluid flow are given in Section 2.2. The numerical solution method for the governing equations is explained in Section 2.3. To accommodate freely floating rigid bodies, the numerical solution method is extended with a strong coupling in Section 2.4.

2.1. Introduction

This section first introduces the reader to some core concepts of the numerical method. This is done by comparing the original and new state of the method in § 2.1.1 and § 2.1.2, respectively. The description of the original state contains a brief summary of the numerical method with references to the rest of this chapter or the appendices. In the description of the new state of the method the additions are introduced.

2.1.1. Description of the original method

The most thorough description of the original method is found in (van der Eijk, 2018), and most recent (unpublished) descriptions in (van der Eijk and Wellens, 2021a,b). Modeling the fluid dynamics is done according to a finite-volume method based on the Navier-Stokes equations. Different phases are modeled as an aggregated fluid with varying properties, described by only one continuity and one momentum equation as given in Section 2.2. The velocity and pressure and pressure fields are therefore assumed continuous over the contact discontinuity.

The governing equations are discretised on a structured grid in a staggered way, where the pressure is defined in the cell center and the velocities on the cell faces as in Figure 2.1b. The spatial discretisation of terms in the momentum equation was left untouched in this work. During the description of the solution method in Section 2.3, the reader will be referred to corresponding texts for spatial discretisation of the terms.

The solution method is a pressure-based method. For integrating the discretised momentum equations over time, a Forward Euler scheme is used. An intermediate velocity is obtained from the explicit evaluation of momentum terms, which is used to find the pressure at the new time level. This pressure

is solved with a Poisson equation that is obtained by substituting the divergence of the new velocity update into the discrete continuity equation. The velocities at the new time level are then calculated from the implicitly determined pressure.

A general description of the methods for tracking and displacing interfaces is given in Appendix B. Tracking and displacing the fluid-fluid interface is done with the PLIC-VoF method by Youngs (1984). Cell labeling is used to help keep a sharp description of the free surface. The cell labeling depicted in Figure 2.1a is a simplification of what is actually used in the method (van der Eijk and Wellens, 2021b), but it should give the reader an idea of how this can be used to apply sets of rules to different neighbouring cell configurations.

Because the definition of the VoF-variable F is important for the readability of the rest of this chapter, it is given in Eq. (2.1). Here F_b is the fraction of the computational cell open to fluids and F_s is the fraction of the computational cell filled with (aerated) water phase, see Figure 2.1b.

$$F = \frac{F_s}{F_b} \quad \text{with} \quad 0 \leq F_s \leq F_b \leq 1 \quad (2.1)$$

In a regular cell without a solid body, the fluid control volume is the full computational cell ($F_b = 1$). Solid geometries are modeled as a nondeformable body of fluid, and the same PLIC-VoF method with cell labelling is used for the description of the interface. An extra step is taken after the reconstruction by defining cut-cells with cell face apertures, depicted as A_x and A_y in Figure 2.1b. The spatial discretisation of the equations inside cut-cells is done similar to that in (Fekken, 2004). The treatment of the fluid-body interface is further discussed in Appendix B.

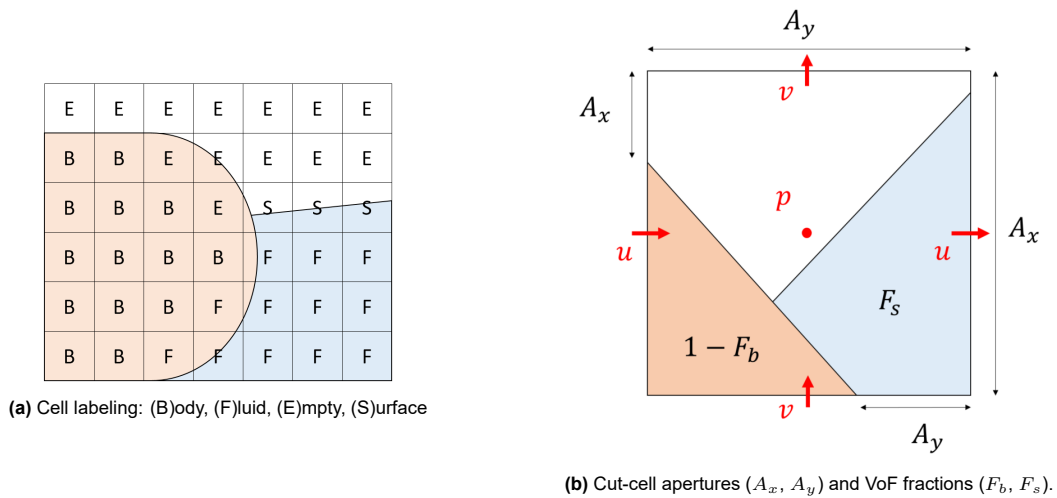


Figure 2.1: Schematic depiction of cell labeling, geometry reconstruction and VoF fractions

2.1.2. New state of the method

Most of the solid geometry modeling was left the same as in the original method. However, several adaptations were made during the time of this work to the modeling of solid bodies that were important for translating bodies in arbitrary direction. The displacement of solid bodies was originally done with an unsplit displacement algorithm, but diagonal motion resulted in mass loss. During this work, the split displacement algorithm for the fluid was also applied to the solid body to overcome this in § B.2.2. Cell labelling in internal body cells was also adapted, which is discussed in § B.2.3.

While the original method allowed prescribed motion of bodies, body velocity update equations still

had to be implemented. In Section 2.4 a new strong coupling is introduced that remains stable during impacts on freely floating rigid bodies.

The above concerns the most important additions to the internal flow model related to the aim of this work. As mentioned earlier, additions to the external boundary conditions are described in Chapter 3. Any other additions that do not fit these two categories are included in Appendix D.

2.2. Governing equations

This section introduces the governing equations that are solved for the aggregated fluid. These are the Navier-Stokes equations for mass and momentum conservation in partial differential conservative form, and a separate transport equation for VoF-variable F :

$$\frac{\partial \rho}{\partial t} + \nabla \cdot (\rho \mathbf{u}) = 0, \quad (2.2)$$

$$\frac{\partial (\rho \mathbf{u})}{\partial t} + \nabla \cdot (\rho \mathbf{u} \mathbf{u}) + \nabla p - \nabla \cdot \left(\mu (\nabla \mathbf{u} + \nabla \mathbf{u}^T) - \frac{2}{3} \mu \nabla \cdot \mathbf{u} \right) - \rho \mathbf{f} = \mathbf{0}, \quad (2.3)$$

$$\frac{\partial F}{\partial t} + \mathbf{u} \cdot \nabla F = 0. \quad (2.4)$$

In these equations, ρ is the aggregated fluid density in the control volume, $\mathbf{u} = (u, v)^T$ is the fluid velocity, p is the fluid pressure, μ is the dynamic viscosity, and \mathbf{f} is the term containing external forces on the fluid. The transport equation used here assumes that the volume change of water due to compressibility is negligible, see also § B.2.1.

2.2.1. Continuity equation

The aggregated fluid density is used to conserve mass of the three separate fluids in the domain: Liquid water, air mixed as bubbles in water and air above the free surface. Equation (2.2) can be written as:

$$\frac{1}{\rho} \frac{D\rho}{Dt} + \nabla \cdot \mathbf{u} = 0. \quad (2.5)$$

The reader is expected to be familiar with the model for the mixture density as introduced in the theoretical model in § 1.1.3. It models the water density in a cell as a homogeneous mixture of liquid density ρ_l and gas density ρ_g , defined by the volume fraction of dispersed air β . These three different fluids make up the mass in a control volume:

$$\rho = \underbrace{(1 - F) \rho_a}_{\text{Air phase}} + \underbrace{\beta F \rho_g}_{\text{Air in mixture}} + \underbrace{(1 - \beta) F \rho_l}_{\text{Liquid in mixture}} = (1 - B) \rho_a + B \rho_l \quad (2.6)$$

Here $B = (1 - \beta) F$ is the amount of liquid in the control volume. Note that the assumption $\rho_g = \rho_a$ is made here, which means that the air density above and inside the mixture are assumed equal in a finite control volume. The full derivation of the material derivative of the density (van der Eijk, 2018) is quite lengthy and is therefore included in Appendix C. In short, the material derivative is found by assuming isentropic flow and using the adiabatic equation of state:

$$\frac{Dp}{Dt} = \left(\frac{\partial p}{\partial \rho_i} \right)_{s_i} \frac{D\rho_i}{Dt} = c_i^2 \frac{D\rho_i}{Dt} \quad \text{for } i = l, a \quad (2.7)$$

and solving for the material derivatives of F and β first. After solving for the necessary terms, the material derivative of the density takes the form:

$$\frac{D\rho}{Dt} = (1 - B) \frac{D\rho_a}{Dt} + B \frac{D\rho_l}{Dt} + H(1 - B)(\rho_l - \rho_a) \nabla \cdot \mathbf{u} \quad (2.8)$$

Here $H(\rho_a, \rho_l, c_a, c_l, \beta, F)$ is a large term found when solving for the material derivative of F . Substituting this in Eq. (2.5) gives the continuity equation that is used in the numerical solver:

$$\frac{1 - B}{C} \frac{D\rho_a}{Dt} + \frac{B}{C} \frac{D\rho_l}{Dt} + \nabla \cdot \mathbf{u} = 0, \quad (2.9)$$

where

$$C = \rho + H(1 - B)(\rho_l - \rho_a). \quad (2.10)$$

2.3. Solution method

The previous section introduced the governing equations for the aggregated fluid, and this section will give the numerical solution method. The solution method used in EVA is a pressure-based method, where the continuity equation contains compressible terms based on the void fraction. The sequence of variable calculation is first explained in § 2.3.1, where the reader will be referred to corresponding contents in the rest of this section.

2.3.1. Sequence of variable calculation

The scheme in Figure 2.2 shows the approximate order of calculations during a time step, and the information exchange between different layers. These layers, from top to bottom, can be described as:

- The fluid conservation layer for conservation of fluid mass and momentum.
- The fluid mass transport layer for advecting the free-surface.
- The solid body transport layer for advecting solid bodies.

We will briefly discuss these layers in this order under the following bold headers.

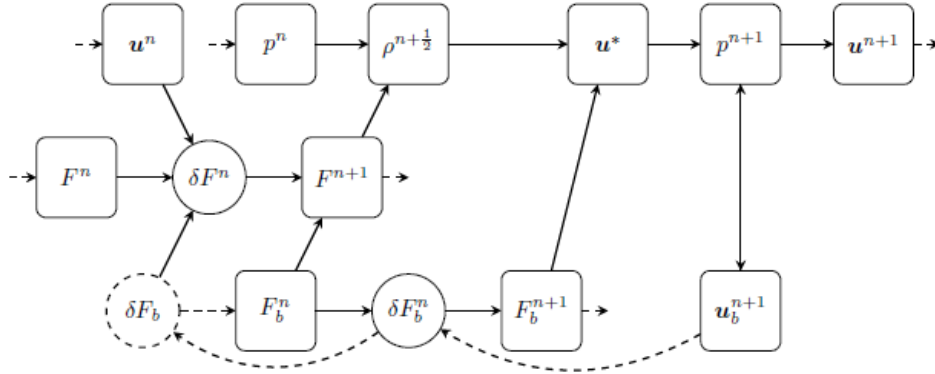


Figure 2.2: Sequence of variable calculation

The fluid conservation layer

The items in the top row of Figure 2.2 approximately represent the contents of this section. They will be discussed in chronological order with references to their respective subsection.

1. The velocity field u^n is known at the beginning of the timestep, as is the pressure p^n . Based

on p^n and VoF-variable F^n , the densities ρ^n are calculated at the beginning of the time step as explained in § 2.3.2.

2. After displacement of the free surface, $\rho^{n+\frac{1}{2}}$ can be calculated based on the new fluid distribution F^{n+1} and p^n . This new density estimate is used in the calculation of an intermediate velocity \mathbf{u}^* . It contains the terms in the momentum equation that are evaluated explicitly, some of which are discretised based on the new position solid boundaries F_b^{n+1} . Evaluation of these terms by the Forward Euler scheme is explained in § 2.3.3.
3. The divergence of the velocity update equation is substituted into the discrete continuity equation in § 2.3.4 to obtain the Poisson equation for the pressure. A new pressure field p^{n+1} is then found that satisfies the conservation equations.
4. The final calculation of the new fluid velocity \mathbf{u}^{n+1} is explained in § 2.3.5. Based on a CFL condition for this new velocity, the time step may be repeated to ensure stability of the Forward Euler scheme in the momentum equation.

The fluid mass transport layer

The middle row of Figure 2.2 represents the displacement of the free surface by VoF-variable F . It is displaced explicitly at the beginning of the time step with the known velocity \mathbf{u}^n . For information on this procedure, see Appendix B.

The solid body transport layer

The bottom row of Figure 2.2 represents the displacement of the body fraction F_b . It is displaced explicitly with known body velocity \mathbf{u}_b^n . This is also discussed in Appendix B. The update equation for the new body velocity \mathbf{u}_b^{n+1} can be strongly coupled to the new pressure p^{n+1} , as will be described in Section 2.4 on fluid-structure interaction.

2.3.2. Density of water and air

Densities of pure water and air are calculated in each cell at the beginning of the time step as a function of the pressure p^n with respect to the atmospheric pressure p_0 . The pure water density is calculated based on the acoustic equation of state:

$$\rho_l^n = \rho_{l,0} + (p^n - p_0) \frac{1}{c_{l,0}^2} \quad (2.11)$$

The pure air density is calculated based on the polytropic energy equation of state (Wemmenhove, 2008, Section 4.2):

$$\rho_a^n = \begin{cases} \rho_{a,0} \left(\frac{p^n}{p_0} \right)^{\frac{1}{\gamma}}, & \text{if } p^n \geq p_0, \\ \rho_{a,0} \left(1 + \frac{2}{\pi} \arctan \left(\frac{\pi}{2} \frac{p^n - p_0}{p_0} \right) \right)^{\frac{1}{\gamma}}, & \text{if } p^n < p_0 \end{cases} \quad (2.12)$$

2.3.3. Intermediate velocity

A Forward Euler scheme is used for the conservative form of the momentum equation, where the densities are kept inside the unsteady velocity term. The control volumes for the discretisation of this equation are on the cell faces where the velocities are defined. The time-discrete momentum equation in this form is shown here:

$$\frac{\rho^{n+\frac{1}{2}} \mathbf{u}^{n+1} - \rho^n \mathbf{u}^n}{\delta t} + \nabla p^{n+1} + \left[\nabla \cdot (\rho \mathbf{u} \mathbf{u}) - \nabla \cdot \left(\mu (\nabla \mathbf{u} + \nabla \mathbf{u}^T) - \frac{2}{3} \mu \nabla \cdot \mathbf{u} \right) - \rho \mathbf{f} \right]^n = \mathbf{0} \quad (2.13)$$

The pressure at the new time level p^{n+1} is calculated implicitly by solving a Poisson equation, as described in § 2.3.4. The density at the new time level is unknown, so an explicit approximation $\rho^{n+\frac{1}{2}}$ is done according to Eq. (2.6) based on the old pressure and the new free surface $\rho^{n+\frac{1}{2}} = \rho(p^n, F^{n+1})$. From Eq. (2.13) we write the following adapted velocity update equation:

$$\mathbf{u}^{n+1} + \delta t \left(\Omega_f^{n+1} \right)^{-1} \frac{1}{\rho^{n+\frac{1}{2}}} \mathbf{G}^{n+1} \delta p = \mathbf{u}^* \quad (2.14)$$

Here \mathbf{u}^* is an intermediate velocity, $\delta p = p^{n+1} - p^n$ the pressure update, \mathbf{G}^{n+1} the discrete gradient operator based on new body position, and Ω_f^{n+1} are the sizes of the momentum control volumes defined on the cell faces like the velocities. The intermediate velocity shows the treatment of separate terms in the momentum equation:

$$\mathbf{u}^* = \frac{1}{\rho^{**}} \left(\rho^n \mathbf{u}^n - \delta t \left(\Omega_f^{n+1} \right)^{-1} \mathbf{C}(\rho^* \{ \mathbf{u}, \mathbf{u}_b \}) \mathbf{u} \right) + \delta t \left(\Omega_f^{n+1} \right)^{-1} \frac{1}{\rho^{n+\frac{1}{2}}} (\mathbf{D}\mathbf{u} + \mathbf{f})^n \quad (2.15)$$

Here ρ^* and ρ^{**} are auxiliary density predictions and \mathbf{C} and \mathbf{D} the discrete convective and diffusive operators. The auxiliary densities replace $\rho^{n+\frac{1}{2}}$ for some terms and are calculated with an additional mass equation based on the VoF mass fluxes as in (Zuzio et al., 2020). This is to achieve consistent coupling between mass and momentum fluxes, which is important for accurate free surface displacement in high density ratio two-phase flows. The form used here is a slight adaptation by van der Eijk and Wellens (2021b) compared to (Zuzio et al., 2020). The quaterd-based method described by van der Eijk and Wellens (2021b) is used to approximate densities at the cell faces, where they are required.

The spatial discretisation of the convective term is done with the first-order upwind scheme as in (Fekken, 2004). For the discretisation of the diffusion term and surface tension in the external force term see (van der Eijk and Wellens, 2019).

2.3.4. Poisson equation for the pressure

Since this method is pressure-based, the pressure is determined first. The new pressure is solved by substituting the divergence of the velocity update Eq. (2.14) into the continuity equation Eq. (2.9), which is first discretised in time:

$$\begin{aligned} & \left(\frac{B}{C} \right)^n \left(\frac{\rho_l^{n+1} - \rho_l^n}{\delta t} + \nabla \cdot (\mathbf{u} \rho_l^n) - \rho_l^n \nabla \cdot \mathbf{u} \right) + \\ & \left(\frac{1-B}{C} \right)^n \left(\frac{\rho_a^{n+1} - \rho_a^n}{\delta t} + \nabla \cdot (\mathbf{u} \rho_a^n) - \rho_a^n \nabla \cdot \mathbf{u} \right) + \\ & \nabla \cdot \mathbf{u}^{n+1} = 0. \end{aligned} \quad (2.16)$$

As the new densities ρ_l^{n+1} and ρ_a^{n+1} are unknown, they will be related to the new pressure p^{n+1} . The material derivative of the density in the aerated water mixture is rewritten to a material derivative of the pressure by substitution of Eq. (2.7). The remaining material derivative of the density of the free air phase is left as is, except the unsteady term is replaced by this discrete form of the acoustic equation of state:

$$\rho_a^{n+1} - \rho_a^n = (p^{n+1} - p^n) \frac{1}{(c_a^2)^n}, \quad \text{with} \quad (c_a^2)^n = \frac{\gamma p^n}{\rho_a^n} \quad (2.17)$$

The divergence of the velocity $\nabla \cdot \mathbf{u}$ also includes the body velocity in cut-cells according to the discretisation in (Fekken, 2004, Eq. 2.12). The discrete form of this divergence is then written as:

$$\nabla \cdot \mathbf{u}^{n+1} = \mathbf{M}_0^{n+1} \mathbf{u}^{n+1} + \mathbf{M}_b^{n+1} \mathbf{u}_b^{n+1}. \quad (2.18)$$

Both discrete divergence operators M_0^{n+1} and M_b^{n+1} are a function of the cut-cell face apertures at the new time level depicted in Figure 2.1b. Applying M_0^{n+1} to the velocity update Eq. (2.14) gives:

$$M_0^{n+1} \mathbf{u}^{n+1} = M_0^{n+1} \mathbf{u}^* - \delta t M_0^{n+1} \left(\Omega_f^{n+1} \right)^{-1} \frac{1}{\rho^{n+\frac{1}{2}}} \mathbf{G}^{n+1} \delta p. \quad (2.19)$$

This discrete update is substituted into Eq. (2.16) using Eq. (2.18). By relating the unknown densities to the new pressure using linearized equations of state, the Poisson equation for the pressure difference $\delta p = p^{n+1} - p^n$ is obtained:

$$\begin{aligned} \left[COMP + \delta t M_0^{n+1} \left(\Omega_f^{n+1} \right)^{-1} \frac{1}{\rho^{n+\frac{1}{2}}} \mathbf{G}^{n+1} \right] \delta p = & M_0^{n+1} \mathbf{u}^* + M_b^{n+1} \mathbf{u}_b^{n+1} \\ & + \left(\frac{B}{C} \right)^n (\nabla \cdot (\mathbf{u} \rho_l^n) - \rho_l^n \nabla \cdot \mathbf{u}) \\ & + \left(\frac{1-B}{C} \right)^n (\nabla \cdot (\mathbf{u} \rho_a^n) - \rho_a^n \nabla \cdot \mathbf{u}) \end{aligned} \quad (2.20)$$

Here *COMP* contains the compressible terms at the left-hand side of the equation. These are the result of applying the equations of state to the unsteady density terms in Eq. (2.16). The time levels of the divergence operators ∇ and velocities \mathbf{u} in the compressible terms at the right-hand side are still subject to investigation. For now, these terms are discretised as $M_0^{n+1} \mathbf{u}^* + M_b^{n+1} \mathbf{u}_b^n$.

2.3.5. New velocity and CFL controller

The new velocity \mathbf{u}^{n+1} is found from filling in Eq. (2.14). The velocities are tested with respect to a CFL condition to ensure stability of the explicit time-integration of the momentum equation. If any velocities exceed this condition, the time step is repeated from § 2.3.3 with a smaller δt . The displacement of the solid body to F_b^{n+1} is recalculated as well for the smaller time step.

2.4. Coupling with body motion

The main objective of this thesis is to add a fluid-structure interaction method to evaluate the effect of aerated water impacts on rigid body dynamics. This section concerns the implementation of a monolithic coupling method, but first a simplified coupling is introduced.

The force exerted by the fluid on a body is calculated by integrating the pressures over the body boundaries. The acceleration of the body is then found from Newton's second law $\mathbf{a}_b = M_b^{-1} \mathbf{f}_b$, where $M_b = M_b$ is a scalar when only considering translational motion. A straightforward coupling of the body motion to the fluid can be achieved by evaluating the forces at time t^n and calculating the acceleration and the new body velocity as

$$\mathbf{u}_b^{n+1} = \mathbf{u}_b^n + \delta t \mathbf{a}_b^{n+1} = \mathbf{u}_b^n + \delta t M_b^{-1} \mathbf{f}_b^n. \quad (2.21)$$

This is referred to as a one-way coupling, which may work in cases where the body motion is clearly dominant over the fluid motion. When this is not the case, such as due to large added mass as described in § 2.4.1, this coupling method might become unstable. Therefore, another coupling method is described in § 2.4.2. Finally, we show in § 2.4.3 how this method can be used when restricting the motion along an arbitrary straight line.

2.4.1. Added-mass effect

This coupling, where the force is treated explicit, may become unstable due to the added-mass effect. A high added-mass ratio (added mass over inertial mass) could cause the body acceleration to diverge. Fekken (2004) explains this by considering a simple hydrodynamical model from added mass potential theory, where the force on the body can be written as

$$\mathbf{f}_b^n = M_a \mathbf{a}_b^n. \quad (2.22)$$

The added mass M_a depends on the shape of the body. Combining Eq. (2.21) and Eq. (2.22) yields the following system for the body acceleration:

$$\mathbf{a}_b^{n+1} = \frac{M_a}{M_b} \mathbf{a}_b^n \quad (2.23)$$

This system is stable only for $M_b > M_a$ so this limits the simulation possibilities to the coupling of heavy objects.

An iterative coupling method can be used to overcome this stability problem, where the body velocity update and pressure update are repeatedly solved until convergence. Using a well-chosen relaxation factor, such an iterative coupling can be stable for a wide range of problems (Fekken, 2004). However, repeatedly solving the pressure Poisson equation is computationally expensive. A coupling method that eliminates this need is described in the next subsection.

2.4.2. Strong coupling

A strong coupling method is introduced that results in stable simulation of floating bodies despite the added-mass effect. It is a monolithic algorithm that treats the pressure force implicit by combining the body velocity update equation into the pressure Poisson equation. Monolithic fluid-structure interaction methods are robust and reliable (Facci et al., 2019; Veldman et al., 2019), and eliminate the need for repeatedly solving the pressure Poisson equation. The robustness stems from the fact that the choice of relaxation factor is important for the convergence of an iterative method, which is not required for a monolithic method.

The body velocity update is written as in Eq. (2.21), except that the acceleration depends on the force in the new time step:

$$\mathbf{w}_b^{n+1} = \mathbf{w}_b^n + \delta t M_b^{-1} \mathbf{f}_b^{n+1}. \quad (2.24)$$

The force on the body can be expressed in terms of gravity and the pressure that has yet to be determined:

$$\mathbf{f}_b^{n+1} = M_b \mathbf{g} + \mathbf{A}_f^{n+1} p^{n+\frac{1}{2}} \quad (2.25)$$

Here \mathbf{A}_f^{n+1} is the body force coupling matrix that includes the cell face apertures and is used to integrate the pressure over the body surface.

The time integration of Eq. (2.24) is according to a Backward Euler scheme, which is used in the simulations throughout this thesis. This method is also implemented as a Crank-Nicolson scheme in a similar manner, which updates the body velocity with an average between \mathbf{f}_b^n and \mathbf{f}_b^{n+1} . To achieve the strong coupling, the body velocity update is integrated into the Poisson equation by combining (2.24)

and (2.25) into

$$\begin{aligned}\mathbf{u}_b^{n+1} &= \mathbf{u}_b^n + \delta t \left[\mathbf{g} + M_b^{-1} \mathbf{A}_f^{n+1} \left(p^{n-\frac{1}{2}} + \delta p \right) \right] \\ &= \mathbf{u}_b^* + \delta t M_b^{-1} \mathbf{A}_f^{n+1} \delta p.\end{aligned}\quad (2.26)$$

Here \mathbf{u}_b^* represents the intermediate body velocity, which contains the known terms of the velocity update and can be placed at the right hand side of the new system of equations:

$$\left[\begin{array}{c|c} \mathbf{A} & \mathbf{Q}_b \\ \hline \delta t M_b^{-1} \mathbf{A}_f^{n+1} & -\mathbf{I} \end{array} \right] \begin{bmatrix} \delta p \\ \mathbf{u}_b^{n+1} \end{bmatrix} = \begin{bmatrix} \mathbf{q} \\ -\mathbf{u}_b^* \end{bmatrix}\quad (2.27)$$

Here $\mathbf{Q}_b \mathbf{u}_b^{n+1}$ is the contribution of the body velocity to the continuity equation.

A disadvantage of this kind of method is that it may increase the system of equations to a very large size when there are more degrees of freedom. The reduction of computational expense becomes much less when a significantly larger system has to be solved. As an example, think of what would happen if a body is allowed to rotate. The velocity of body boundary cells is then no longer uniform, so the number of degrees of freedom increases to the amount of body boundary cells. Since rotation of objects is not considered in the current thesis, this strong coupling method still seems appropriate.

2.4.3. Restricted direction

To restrict fluid-body coupling to an arbitrary direction, like on an axis or around a reference point, the body acceleration can be projected on a unit vector $\hat{\mathbf{t}}$:

$$\bar{\mathbf{a}}_b = (\hat{\mathbf{t}} \cdot \mathbf{a}_b) \hat{\mathbf{t}} = \begin{bmatrix} \hat{t}_x^2 & \hat{t}_x \hat{t}_y \\ \hat{t}_y \hat{t}_x & \hat{t}_y^2 \end{bmatrix} \begin{bmatrix} a_{b,x} \\ a_{b,y} \end{bmatrix} = \mathbf{T}_b \mathbf{a}_b\quad (2.28)$$

The direction of this unit vector determines in which direction the body can accelerate due to gravity and fluid pressure. Setting the tangent unit vector $\hat{\mathbf{t}}$ to $(1, 0)$ or $(0, 1)$ will restrict the acceleration to the x - and y -axis, respectively. Any other positive unit vector $\hat{\mathbf{t}}$ can be chosen to allow acceleration only in one direction. Using coupling direction matrix \mathbf{T}_b , the body velocity update Eq. (2.24) is written as:

$$\mathbf{u}_b^{n+1} = \mathbf{u}_b^n + \delta t \mathbf{T}_b \left(M_b^{-1} \mathbf{f}_b^{n+1} + \mathbf{g} \right).\quad (2.29)$$

Equation (2.26) then becomes:

$$\begin{aligned}\mathbf{u}_b^{n+1} &= \mathbf{u}_b^n + \delta t \mathbf{T}_b \left[\mathbf{g} + M_b^{-1} \mathbf{A}_f^{n+1} \left(p^{n-\frac{1}{2}} + \delta p \right) \right] \\ &= \mathbf{u}_b^* + \delta t M_b^{-1} \mathbf{T}_b \mathbf{A}_f^{n+1} \delta p.\end{aligned}\quad (2.30)$$

Setting $\mathbf{T}_b = \mathbf{I}$ returns the unrestricted body velocity update. Here \mathbf{u}_b^* again contains all the pieces of the equation that are known. A similar system as in Eq. (2.27) can be defined, but now including direction coupling matrix \mathbf{T}_b . Note that any initial velocity given to the body in a direction separate from the coupling direction will remain constant for the duration of the simulation.

3

Wave generation

The secondary objective of this thesis is to add external boundary conditions for wave generation to the numerical method EVA. This will allow validation of the method in breaking wave impact and more types of experiments. In this chapter the implementation of boundary conditions is discussed. First different analytical theories for wave motion are described in Section 3.1 and followed by how the inflow boundary conditions are set accordingly in Section 3.2. Additionally, a method for initialising a periodic wave over the entire domain with periodic boundary conditions is described in Section 3.3.

3.1. Wave theory

The two analytical wave theories that are used for generating waves at the boundary are linear potential Airy wave theory and Rienecker-Fenton non-linear stream function wave theory (Rienecker and Fenton, 1981), discussed in § 3.1.1 and § 3.1.2, respectively. Additionally, the equations for a third-order Stokes wave are included in § 3.1.3, as they will be used for the initialisation of a periodic wave later in Section 4.3.

3.1.1. Linear potential wave

The linear wave velocity potential satisfies the Laplace equation for incompressible flow and the kinematic boundary conditions at the free surface and at the bed. The approximations that are used in this theory are only valid for small amplitude waves (w.r.t. water depth or wave length). For water depth h , a linear wave can be constructed from the wave height H , period T and phase difference ϵ :

$$\Phi(x, z, t) = \frac{H\omega}{2k} \frac{\cosh(k(z+h))}{\sinh(kh)} \sin(kx - \omega t + \epsilon) \quad (3.1)$$

Here wave number k and wave frequency $\omega = 2\pi/T$ are related by the dispersion relation

$$\omega^2 = gk \tanh(kh), \quad (3.2)$$

which follows from the dynamic free surface boundary condition. The free surface elevation is found from the cosine function:

$$\eta(x, z, t) = \frac{H}{2} \cos(kx - \omega t + \epsilon) \quad (3.3)$$

The velocities in the fluid are found from the spatial derivatives of the potential function:

$$\begin{aligned} u_x(x, z, t) &= \frac{\partial \Phi}{\partial x} = \frac{H\omega}{2} \frac{\cosh(k(z+h))}{\sinh(kh)} \cos(kx - \omega t + \epsilon) \\ u_z(x, z, t) &= \frac{\partial \Phi}{\partial z} = \frac{H\omega}{2} \frac{\sinh(k(z+h))}{\sinh(kh)} \sin(kx - \omega t + \epsilon) \end{aligned} \quad (3.4)$$

Velocities at positions above the mean free surface level $z = 0$ are overestimated due to the exponential profile. For this reason, velocities above this level are found by constant extrapolation from $z = 0$ so that:

$$\mathbf{u}(x, z, t) = \mathbf{u}(x, 0, t) \quad \forall \quad z \geq 0$$

A superposition of multiple linear waves allows for the generation of irregular waves. This is achieved by summing the individual linear steady wave potentials, which is equivalent to directly summing the elevation and velocity components.

3.1.2. Rienecker-Fenton wave

A Rienecker-Fenton wave is a non-linear steady wave solution found by Fourier approximation, which is applicable to a wide range of water depths. In the following, all variables are made dimensionless with respect to the water depth h and gravitational acceleration g so that

$$x = x/h, \quad z = z/h, \quad \eta = \eta/h, \quad \Psi = \Psi/\sqrt{gh^3}, \quad c = c/\sqrt{gh}, \quad k = kh = 2\pi h/\lambda.$$

Here x and z are coordinates in the steady wave solution (moving with the wave) and relative to the bed, η is the surface elevation relative to the bed, c the group velocity of the moving wave, k the wave number and λ the wave length. The stream function Ψ is written as a truncated series up to N :

$$\Psi(x, z) = B_0 z + \sum_{j=1}^N B_j \frac{\sinh(jkz)}{\cosh(jkh)} \cos(jkx) \quad (3.5)$$

Here the coefficients B_j are determined by a N -component Fourier approximation of the free surface profile subject to several boundary conditions. For water depth h a non-linear wave can be constructed from the wave height H , period T and phase difference ϵ . The numerical method and boundary conditions to find this solution are described by Rienecker and Fenton (1981).

The shape of the free surface at any arbitrary position and time can be found by computing a N -component Fourier transform of the dimensionless free surface elevation from the Rienecker-Fenton solution ($\eta_m = \eta(x_m)$ with $m = 0, 1, \dots, N$). As η_m is defined relative to the bed, it is first made relative to the mean free surface level by subtracting 1. The coefficients C_j resulting from the Fourier approximation are then used to find the free surface elevation relative to the mean surface level in a coordinate system ($X = x + ct, Z = z$) fixed to the bed:

$$\eta(X, t) = \sum_{j=1}^N C_j \cos(j(k(X - ct) + \epsilon)) \quad (3.6)$$

The velocities in the fluid are found from the stream function with the known coefficients B_j .

$$\begin{aligned} u_x(X, Z, t) &= \frac{\partial \Psi}{\partial z} = c + B_0 + k \sum_{j=1}^N j B_j \frac{\cosh(jkZ)}{\cosh(jkh)} \cos(j(k(X - ct) + \epsilon)) \\ u_z(X, Z, t) &= -\frac{\partial \Psi}{\partial x} = k \sum_{j=1}^N j B_j \frac{\sinh(jkZ)}{\cosh(jkh)} \sin(j(k(X - ct) + \epsilon)) \end{aligned} \quad (3.7)$$

The coefficients B_j and C_j , and the non-dimensional wave number k and group velocity c only have to be determined once at the start of the simulation. The inputs and outputs of Eq. (3.6) and Eq. (3.7) are dimensionless and have to be given a dimension again before they are used in the inflow conditions. For regular wave generation, this non-linear stream function theory is preferred due to its wide range of applicability (Wellens, 2012).

3.1.3. Third-order Stokes wave

A third-order Stokes wave is a nonlinear wave solution to the same equations as for the linear potential wave. The solution is applicable to mildly non-linear waves in deep water. Stokes wave solution is not used for generating regular steep waves at the boundary, because a better alternative is introduced in the next paragraph. It is included here, because this type of wave solution will be used for the initial condition of a periodic wave in Section 4.3. The potential and free surface elevation of the third-order Stokes solution are written as:

$$\begin{aligned} \theta &= kx - \omega t \\ \eta(x, t) &= a \left\{ \left[1 - \frac{1}{16}(ka)^2 \right] \cos \theta + \frac{1}{2}(ka) \cos 2\theta + \frac{3}{8}(ka)^2 \cos 3\theta \right\} \\ &\quad + \mathcal{O}((ka)^4) \\ \Phi(x, z, t) &= a \sqrt{\frac{g}{k}} e^{kz} \sin \theta + \mathcal{O}((ka)^4) \end{aligned} \quad (3.8)$$

The flow velocities are found from the spatial derivatives of the potential as is done in § 3.1.1.

3.2. Inflow conditions

Boundary conditions at the in- and outflow regions can be set using the analytical expressions for wave elevation and flow velocities. A choice is made to use a Dirichlet condition for the velocity, because it gives more control over the fluid fluxes through the wall than a Dirichlet condition for the pressure. Another reason to prescribe velocity instead of pressure is the unknown flow behaviour of air above the free surface. As will be explained in Figure 3.2.2, a relatively simple solution can be used to specify a value for these unknown velocities.

The set of boundary conditions at the inflow consists of normal and tangent flow velocities and the fluid fraction in ghost cells just outside the numerical domain. Non-zero wall normal velocities allow for fluid into and out of the numerical domain, depending on the fluid distribution along the wall. The tangent wall velocity can be set with a no-slip condition, which only has an effect if the fluid is given a viscosity. The following paragraphs describe how the wall velocities and fluid distribution in ghost cells are determined.

3.2.1. Free surface elevation

The fraction distribution in the ghost cell column is set to the height of the free surface (e.g. Eq. (3.3) or Eq. (3.6)) at the location of the wall. This means that all cells below the free surface are completely full and the cell that contains the free surface is filled to that level. All cells above that are empty. The surface inside the ghost cell is reconstructed to be horizontal, so that only the wall velocity determines the volume flux into the domain. A distinction can be made between two phases of inflow conditions during wave motion:

- Fluid flux into the domain when the free surface is rising,
- and fluid flux out of the domain when the free surface is dropping.

During this second phase the out-flux of fluid can not be prescribed exactly, because it depends on the fluid dynamics inside the domain. During a steady regular wave simulation, the dynamics inside the domain will often follow the prescribed wave well enough for this not to be a problem.

3.2.2. Inflow velocities

The horizontal volume flux into the domain is approximated using an analytical horizontal velocity profile (e.g. (3.4) or (3.7)) over the vertical wall. The following three paragraphs explain how this is applied to the inflow boundary below, at and above the instantaneous free surface.

Below the free surface

The velocity profile is approximated to be linear over the height of a cell, so that the wall velocity in that cell is the average of the cell's lower and upper node velocity in Figure 3.1. This method is applied up to the cell that contains the analytical free surface.

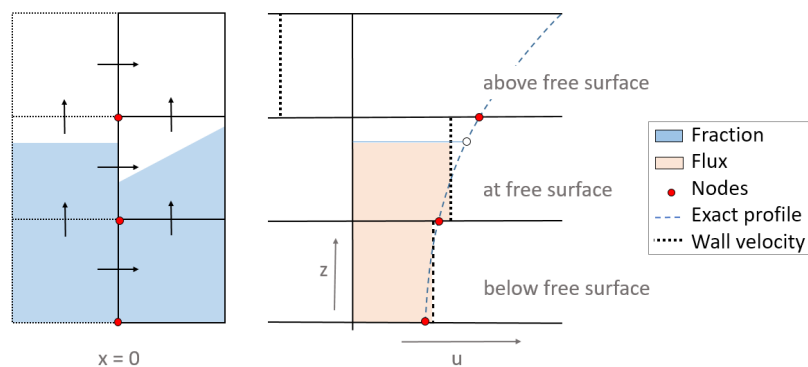


Figure 3.1: Schematic depiction of inflow conditions for wave motion

At the free surface

The fluid fraction inside the free surface cell at the free surface is always between 0 and 1 during inflow. Using the same method as below the free surface can lead to overestimation of the fluid flux into the domain, because the velocity profile should only be integrated up to the free surface. A linear interpolation is used so that the prescribed flux is closer to the analytical value (see white node in Figure 3.1).

Above the free surface

In the second phase (air) above the free surface, the wall normal velocities are not defined by the analytical wave theories that are considered here. During a propagating wave simulation, a sort of

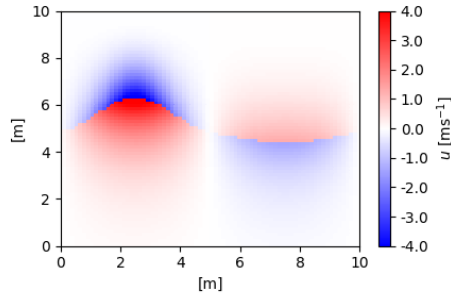


Figure 3.2: Initial horizontal velocity field according to inflow conditions including extrapolated air velocities.

mirrored wave can be observed in the flow of air above the free surface. This mirrored pattern is also used in the inflow conditions, by setting the velocity of air in the opposite direction. These velocities are extrapolated such that they decrease with power $p = 3$ to zero at the top of the domain.

$$u_{air,j} = - \left(\frac{z_{top} - z_j}{z_{top} - \eta} \right)^p u_{fs} \quad (3.9)$$

3.3. Single periodic wave

Since any regular wave is periodic by definition, periodic boundary conditions can be used to propagate a single wave through a numerical domain. In this section the method is described that can be used to generate such a wave.

3.3.1. Periodic boundary conditions

The boundary conditions posed on the left and right wall are as follows:

- At the right wall, the normal velocity is treated as an unknown, which has to be found from a pressure gradient over the outflow wall. The pressure in the ghost cell is solved as if it were the first column of cells on the left wall inside the domain. This is done by changing the Poisson matrix such that the pressures in the ghost cells point to the right hand side values of the left wall interior cells.
- At the left wall, the normal velocity is copied from the right wall. The pressures are solved as they would under regular inflow conditions.

During the time step, all field values such as reconstruction, fluid fraction and so on, are copied from the interior of one side of the domain to the exterior of the other side of the domain.

3.3.2. Initial conditions and air velocity

To approximate a periodic wave solution, the conditions from Section 3.2 for the inflow boundaries are applied over the full domain.

It was found that it is important to set the wave phase exactly so that the horizontal velocities at the walls are zero, as in Figure 3.2. When initialised with an arbitrary wave phase, unphysical pressure fields were found after one time step. Whether this is due to an implementation fault, or whether it has something to do with periodic boundary conditions in general has not been investigated.

To study the effect of extrapolating air velocities the wave of Figure 3.2 is propagated for 1.0 s and compared to the initial condition with zero air velocities. Appendix E shows no observable effect of this initial setting on the fluid velocities after 1.0 s.

3.4. Conclusion

This chapter has introduced the external boundary conditions that are used for generating waves. In Section 3.1 three different analytical theories were given. Then in the approximation of analytic solutions at the boundary was discussed. Finally, in Section 3.3 periodic boundary conditions were discussed and a method for initialising a single periodic wave.

The inflow conditions for a regular Rienecker-Fenton wave will be verified in the numerical experiment in Section 4.2. The single periodic wave will be used to simulate a breaking wave in Section 4.3. A superposition of linear components is used in the generation of a steep focused wave in Chapter 5.

From the propagation of a single period wave in Figure 3.2, the velocity of air seems to have very little effect on the fluid velocities in the wave.

4

Verification and validation

This chapter contains the results of three numerical experiments that were performed to verify and validate the methods for fluid-structure interaction and wave generation. First, in Section 4.1 a simulation of a flat water drop test for a buoyant cylinder is compared to other numerical and physical experiments to verify the fluid-body coupling method. Second, in Section 4.2 regular waves are propagated through a long numerical domain to study the dissipation of energy compared to similar methods. Third, in Section 4.3 a numerical experiment of a breaking wave against a vertical wall is performed and compared to a reference for different aeration levels.

4.1. Buoyant cylinder water entry

This section concerns the numerical simulation of the flat water entry of a buoyant cylinder, see Figure 4.1. The coupling method introduced in Section 2.4, is designed for studying impacts on buoyant rigid marine structures. Facci et al. (2019) propose a different coupling technique for solving the same type of problems relevant to the design of marine vessels. They perform a validation study by comparing to custom designed physical experiments by Russo et al. (2017), which are also used to verify our new coupling method.

First, the experimental and numerical setup is described in § 4.1.1. The results of our incompressible simulations compared to the reference are reported in § 4.1.2. In § 4.1.3 the effect of aeration on the impact dynamics is evaluated. Finally, conclusions are drawn in § 4.1.4 followed by a discussion in § 4.1.5.

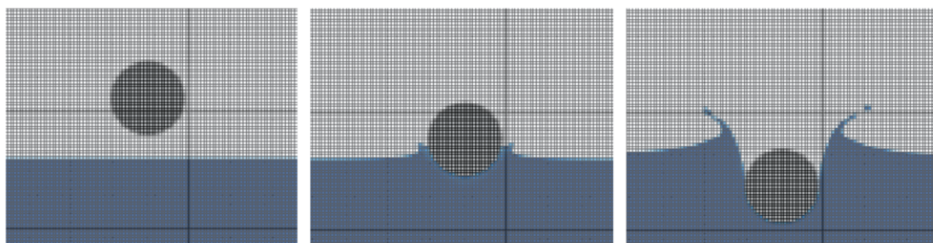


Figure 4.1: Flat water entry of 2D buoyant cylinder

4.1.1. Numerical setup

The slamming experiments performed by Russo et al. (2017) are performed for buoyant cylinders with different masses along a vertical sled into flat water. The penetration over time of the cylinders into the free-surface is obtained from both an accelerometer and a high speed camera. The water basin dimensions in the 2D plane of interest are the basin width $w = 1.5$ m and still water level $d = 0.4$ m. The cylinder has a radius of $r = 0.08$ m, a variable mass m by adding/removing weights, and a length $l = 0.295$ m into the 3rd dimension.

The numerical reference assumes 2D flow and 1-DOF body motion (Facci et al., 2019). The densities and viscosities of water and air are assumed $\rho_{water} = 1000$ kg m⁻³, $\rho_{air} = 1$ kg m⁻³, $\mu_{water} = 10^{-6}$ Pa s and $\mu_{air} = 1.48 \cdot 10^{-5}$ Pa s. Four drop heights ($h = 0.25, 0.50, 0.75, 1.00$ m) and two masses ($m = m_0, m_1 = m_0 + 1$ kg) are considered, where $m_0 = 2.214$ kg.

The simulations in this thesis for all h and m are done with the compressible solver and zero initial aeration level. The cylinder is positioned at $w/4$ from the left to be consistent the physical experiment (Russo et al., 2017). The domain height is 0.75 m and the cylinder is positioned 0.05 m above the free surface with an initial velocity V_0 that should match the reference at impact. This is done so that the cylinder is in free-falling motion before impact, but the entire free-fall trajectory from the drop height h is skipped to save time.

4.1.2. Validation results

The following results are reported here: The impact velocity and the penetration depth over time. Both data are compared to reference experiments.

Impact velocity

A meaningful comparison with reference results can only be made when the impact velocities V_{im} are the same or at least very close to each other. Before the simulations from 0.05 m height were performed, a value for the free-fall acceleration was determined from a full height simulation. The acceleration during free-fall was found to be 9.7 ms⁻², which is faster than the experimental results in Figure 4.2. This is likely due to the friction in the experimental setup, which is not included in the simulation. From the acceleration during free falling, initial velocities V_0 were determined for starting

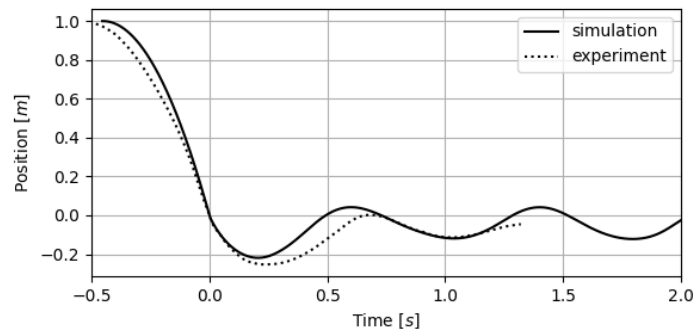


Figure 4.2: Free falling buoyant cylinder from $h = 1.00$ m with $m = m_0 + 1$ kg, compared to physical experiment (Russo et al., 2017).

the simulation at 0.05 m for all comparisons. The recorded impact velocities during the simulations are given in Figure 4.3, and they are very close to the reference.

Penetration depth

Time series of the penetration of the cylinder through the free-surface are shown in Figure 4.4, where ξ is the position of the lowest point of the cylinder with respect to the still water level. The results

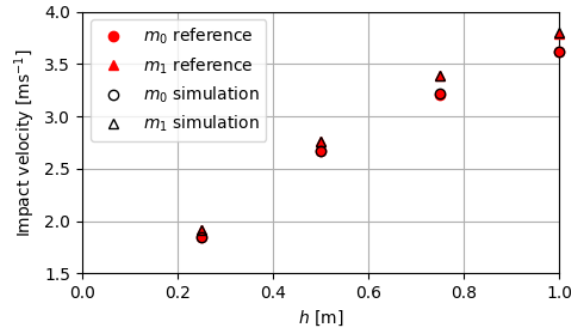


Figure 4.3: Impact velocities V_{im} recorded during the simulations, compared to physical experiment (Russo et al., 2017).

presented are all for a resolution of 21 cells per diameter of the cylinder. All figures in Figure 4.4 show

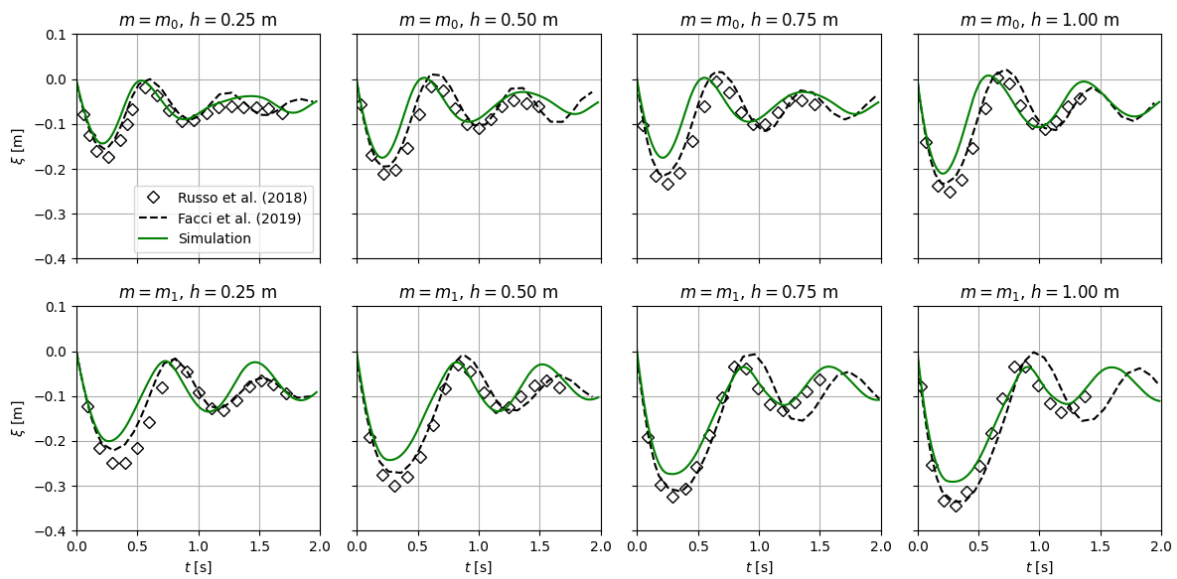


Figure 4.4: Penetration through the free surface compared to physical and numerical experiments of Russo et al. (2017) and Facci et al. (2019).

that the maximum penetration depth is underestimated. While it was expected that the assumption of fully 2D flow would cause an overestimation of the impact forces (Facci et al., 2019), the observed differences are quite large. Possible causes were investigated in § 4.1.5.

Despite the underestimation of penetration depth, the coupling method is able to remain stable during repeated water entry and exit in the buoyancy oscillations after impact. The frequencies of these oscillations in Figure 4.4 show reasonable similarity to the reference results. Wall effects and collapsing water on top of the cylinder after impact make it hard to compare the results after the first impact.

4.1.3. Influence of aeration

To evaluate the effect of aerated water on the rigid body dynamics during and after impact, the simulation for $m = m_1$ and $h = 1.00$ m is repeated for initial void fractions $\beta = 0.001, 0.01, 0.05$ and 0.10 . We call this set the aerated impacts. Additionally, the simulation is repeated for $\beta = 0$ with reduced water densities $\rho_l = 999, 990, 950$ and 900 kg m⁻³, that correspond approximately to the mixture densities of the above void fractions. We call this set the reduced density impacts. With this, it is hoped that

the cushioning effect of aerated water compressibility can be isolated from the effect of the reduced mixture density.

Figure 4.5 shows the dimensionless vertical force on the rigid body during impact. The left figure shows oscillating loads after the aerated impact, which is caused by wall-reflecting pressure waves as will be shown later in Figure 4.7.

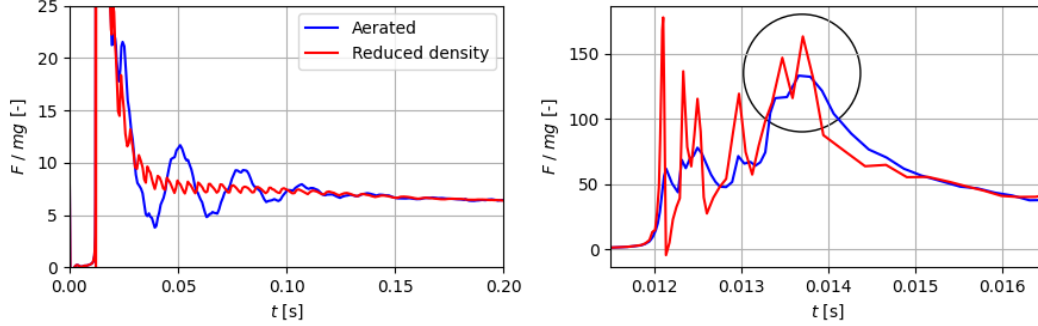


Figure 4.5: Dimensionless vertical force during impact with aeration $\beta = 0.05$ and reduced density $\rho = 950 \text{ kg m}^{-3}$. Right figure zooms in on the missing peak of the left figure. The black circle indicates the sustained impact force.

For the cushioning effect, we are more interested in the initial impact shown at the right of Figure 4.5. We distinguish between the initial impact force, which is the first large peak, and the sustained impact force, which is circled in black.

To quantify the cushioning effect during these simulations, two maximum forces F_β and F_ρ are defined for the aerated impacts and reduced density impacts, respectively. The aerated force F_β is the maximum force during $\beta > 0$ impacts with $\rho_l = 1000 \text{ kg m}^{-3}$. The reduced density force F_ρ is the maximum force during $\beta = 0$ impacts at $\rho_l = \rho(\beta)$ according to the mixture density. The ratio between the two for different void fractions is shown in Figure 4.6. The horizontal axis contains the cylinder entry Mach number M_{ce} defined as:

$$M_{ce} = \frac{V_{im}}{c_w(\beta)} \quad (4.1)$$

The impact velocity $V_{im} = 3.7 \text{ m s}^{-1}$ was given for this simulation in Figure 4.3. The speed of sound c_w is calculated from Eq. (1.3) using the initial void fraction of each simulation.

In Figure 4.6a a significant initial impact force reduction due to the compressibility of aerated water is shown, even when corrected for the reduced fluid density. The initial impact peak in Figure 4.5 looks a bit irregular and it is suspected that its extreme height might be some sort of numerical artifact.

To solidify the belief that the effect of compressibility is significant, the same comparison is made in Figure 4.6b for the sustained impact force as defined in Figure 4.5. Despite the correction for the reduced density of the aerated water mixture, the compressibility still reduces the peak load for increasing M_{ce} . The compressibility of aerated water reduces the impact force by approximately 8% at 1% aeration and by 19% at 5% aeration when $V_{im} = 3.7 \text{ m s}^{-1}$. The reduction is even greater when comparing to zero aeration impact without reduced density correction.

The maximum depth of penetration during reduced density simulations and during aerated simulations remained within 0.3% of each other. The effect of compressibility due to aeration on the global displacement of the rigid body can be neglected for this range of cylinder entry velocity Mach numbers.

Pressure oscillations were observed in the bottom left corner of the numerical domain, which is closest to the cylinder location of impact. The pressure signal in Figure 4.7 has similar oscillation frequency as the force on the cylinder after impact in Figure 4.5. The intensity of the pressure wave in the corner of the closed domain increases due to aeration.

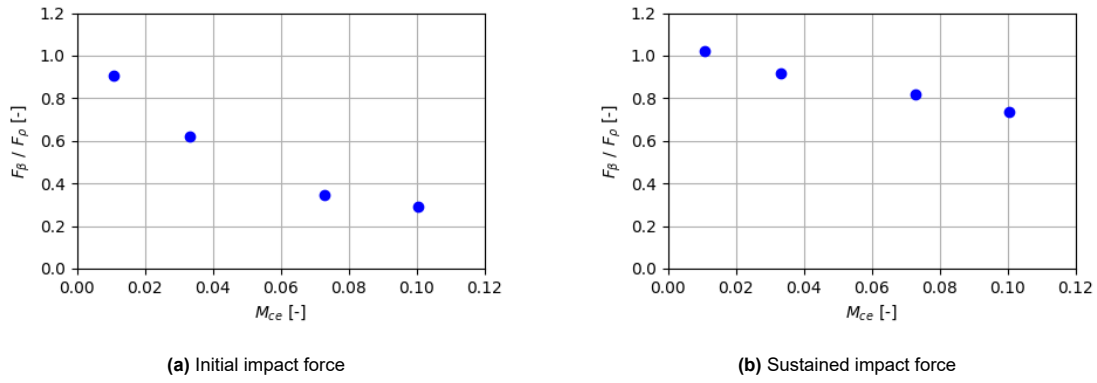


Figure 4.6: Maximum force during aerated water impact (F_β) relative to the maximum impact force during reduced density impact (F_ρ) for increasing cylinder entry Mach number M_{ce} .

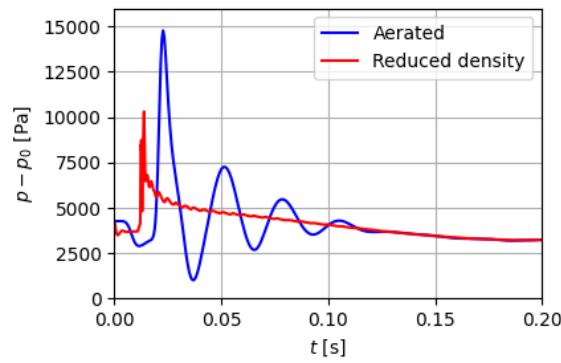


Figure 4.7: Gage pressure at left bottom corner of the domain during aerated impact with $\beta = 0.05$ and during reduced density impact with $\rho_l = 950 \text{ kg m}^{-3}$.

4.1.4. Conclusion

A numerical experiment of buoyant cylinder impact was performed for impact velocities V_{im} between $1.8\text{-}3.7 \text{ m s}^{-1}$ and two different masses in Figure 4.4. The newly implemented monolithic coupling method is able to remain stable for the simulation of buoyant bodies, where a one-way coupling would become unstable. The penetration depth after impact is consistently underestimated compared to the references.

The simulation with the highest impact velocity $V_{im} = 3.7 \text{ m s}^{-1}$ was repeated for various aeration levels corresponding to entry velocity Mach numbers M_{ce} up to 0.1. With regard to the effects of aeration on cylinder slamming, the following conclusions are drawn:

- The maximum depth of penetration after impact is affected most by the reduced density of the aerated mixture, not by the increased compressibility.
- During impact with entry Mach number $M_{ce} = 0.074$, the sustained impact force is reduced in Figure 4.6b due to the compressibility of aerated water. The reduction is 8% and 19% for void fractions $\beta = 0.01$ and 0.05, respectively.
- Pressure waves from the initial impact in aerated water with $\beta = 0.05$ almost double the intensity of the reflected pressure in the corner of the domain in Figure 4.7.

4.1.5. Discussion

In this subsection we discuss the limited penetration depth compared to the reference experiments. Also the convergence of results for increasing cell resolutions is discussed at the end.

Penetration depth

Three possible causes were identified for the difference in penetration depth between presented and reference results:

1. The use of the compressible solver compared to an incompressible solver as in the reference.
2. The modeling of fluid and body surface at the moment of impact.
3. Wall effects due to the choice of numerical domain setup.

The first cause is tested by performing the same simulation with the fully incompressible solver. No observable difference is found with respect to the rest of the results. This means that the limited penetration depth is not a consequence of the compressible treatment of the air phase.

It was found that the maximum impact force occurs at $y = 5 \cdot 10^{-3}$ m above the free-surface consistently for all simulations in Figure 4.4. This may due to the body surface and fluid surface arriving in the same cell and triggering the impact. Assuming that the reference impacts occur exactly at $y = 0.0$ m, a penetration difference of $\Delta y_{\max} = 5 \cdot 10^{-3}$ m could be explained this way. However, subtracting this from all the results still leaves a gap in the comparison.

To test the influence of wall effects, another simulation for $h = 1.0$ m and $m = m_0 + 1$ kg is done with the cylinder in the middle of the domain. The maximum penetration is found to be very similar in Figure 4.8, but the subsequent oscillations show very different behavior. Wall effects are significant for the buoyancy oscillations after the maximum penetration.

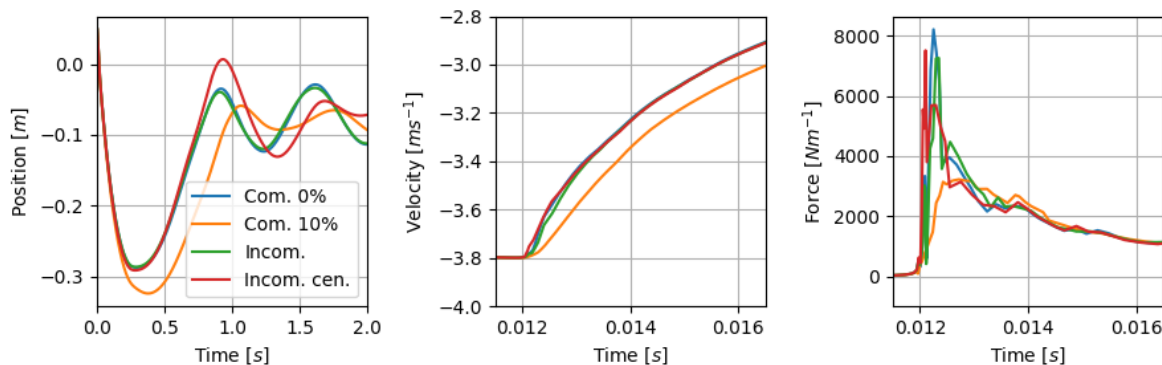


Figure 4.8: Penetration depth, impact velocity and force for different solver and domain settings.

Grid convergence

No grid-independent solution was found for the case. Figure 4.9 shows penetration depth and impact force for different resolutions in *cells per diameter* of the cylinder. The maximum penetration actually seems to diverge for increasing resolution, and the timing of the impact force contains large differences. The timing difference is likely explained by the surface reconstruction as discussed in § 4.1.2. The study for grid convergence was not performed properly due to varying time step, but the diverging behavior for increased resolution shows the sensitivity small differences. The exact origin of the differences has not been found, but it is expected be caused by grid-related sensitivities such as cell-merging or surface reconstruction. This should be considered when determining a confidence interval for the results of coupled motion simulations.

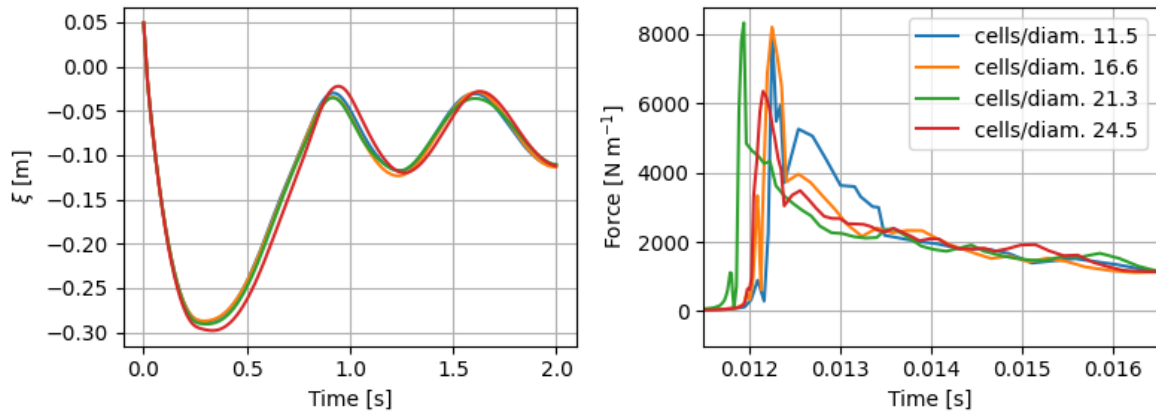


Figure 4.9: Penetration depth and impact force for different cylinder resolutions.

4.2. Regular wave propagation

A regular wave propagation experiment is performed to verify the wave inflow conditions of Section 3.2. While the numerical method is not designed for propagating waves, an insight in the wave energy dissipation can be used to better approximate wave heights at impact zones. The numerical setup is described first in § 4.2.1. The free surface and velocity profile are compared to reference material in § 4.2.2. Wave height dissipation is discussed in § 4.2.3. Finally, conclusions are drawn in § 4.2.4.

4.2.1. Numerical setup

The propagating wave is simulated twice; once with the conservative treatment of the convective fluxes as described in § 2.3.3 and once with non-conservative treatment of these fluxes. The implementation of the conservative treatment of the momentum fluxes was not part of this project, but it was found to be quite important for the free-surface behaviour in some of the experiments that were performed. So, the current experiment is used to quantify its effect in reducing energy dissipation during wave propagation.

The simulations are done for a wave with the same parameters as (Wellens, 2012, Table 4.2). In that study, a Rienecker-Fenton wave with a period of 6 s and wave height of 4 m is propagated using the one-phase free-surface flow method in ComFLOW. Unlike the reference, a uniform grid was used in both directions according to Table 4.1. The maximum simulation time is 150 s for these specific wave parameters, so that reflection from the closed domain wall does not influence the results.

Parameter	Value
Water depth	10 m
Domain height	15 m
Nr. of vertical cells	17
Domain length	1500 m
Nr. of horizontal cells	1500
Time step	CFL condition
Simulated time	150 s

Table 4.1: Simulation parameters for Rienecker-Fenton wave propagation.

4.2.2. Free surface and velocity profile

In the left of Figure 4.10 the free surface profile of the first two wave lengths is compared to the Rienecker-Fenton solution in § 3.1.2. The overall shape compares reasonably well, especially when

considering the coarse numerical grid size indicated by the horizontal grid lines of the figure. This suggests that the weighted averaging in the free surface cell as described in Section 3.2 works well for coarse grids. Finer grids were not simulated for practical CPU reasons.

The discrete horizontal velocity profiles in the propagating wave are shown on the right of Figure 4.10. After approximately two wavelengths the velocity already deviates quite a bit from the prescribed solution. It is expected that this will improve with increasing grid resolution, but differences might still persist as in (Wellens, 2012, Fig. 5.11b).

The reverse velocities of air above the free surface of the propagating wave solution can clearly be distinguished. Only a minimal difference was observed when prescribing the extrapolated air velocities as described in Section 3.2. Simply setting the air velocity to zero actually resulted in slightly better approximation of the horizontal velocity profile, suggesting that the additional shearing velocities at inflow may cause some extra dissipation.

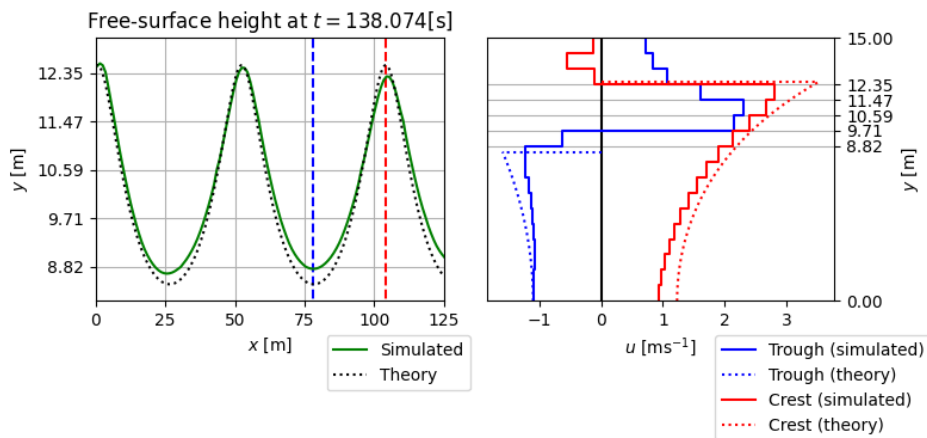


Figure 4.10: Free surface profile of first two wave lengths (on the left) and the horizontal velocity profile (on the right) in a crest and a trough at the positions indicated by the corresponding colored vertical lines in the left figure. The positioning of horizontal grid lines is equal to the numerical cell spacing.

4.2.3. Wave height dissipation

In the left of Figure 4.11 a snapshot of the free surface profile in the first 500 m is taken at $t = 138$ s. The vertical axis ζ is the wave elevation with respect to the free surface. The dotted lines represent results of Wellens (2012), where the lower and higher wave heights are the original and the improved method. A clear pattern is observed where the wavelength decreases with waveheight, and this pattern is consistent over both the reference and presented results.

By making a dimensionless figure of $H(x) / H_0$ versus x / λ , the wave height dissipation over wave length can be visualised clearly and compared to reference results. Here $H(x)$ is the wave height at position x , H_0 the wave height at $x = 0$, and λ the wave length. The comparison is made with the one-phase flow results of (Wellens, 2012, Fig. 4.17) and with the two-phase flow results of (Wemmenhove, 2008, Fig. 5.10a) in the right of Figure 4.11. The latter simulated a different wave with a height of 3.0 m and a period of 6.0 s at depth 30.0 m, but it is still included for qualitative comparison.

The presented new simulations have been done with a Forward Euler scheme in time and a first-order upwind scheme in space. A significantly reduced dissipation is observed when using the mass conservative treatment of momentum fluxes. The order of the reduction is similar to that achieved by different improvements in both references. In the one-phase flow method by Wellens (2012) the reduction is achieved by a Lax-Wendroff method with flux limiters. In the two-phase flow method by

Wemmenhove (2008) the reduction is achieved by a second-order Adams-Bashforth scheme with a second-order upwind scheme. It is expected that the dissipation in this method will be further reduced when also applying these second-order schemes.

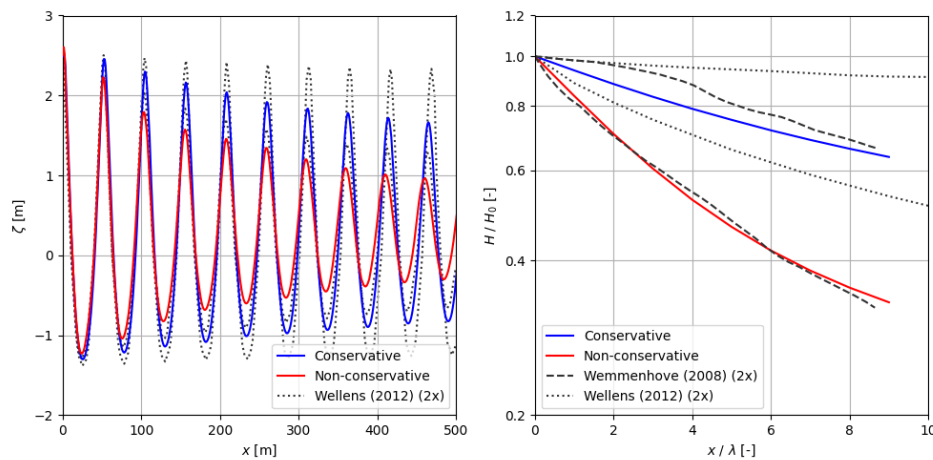


Figure 4.11: Free surface profile of Rienecker-Fenton wave over the first 500 m (on the left) and the relative wave height dissipation (on the right).

4.2.4. Conclusion

The implementation of the inflow conditions in Section 3.2 below and in the free surface have been verified by the propagation of a regular wave in a long domain. The free surface and horizontal velocity profiles further in the domain compare reasonably well to theory, considering that the wave height is contained in approximately four grid cells in Figure 4.10. It was also found that extrapolating the air velocities in the inflow conditions as in Section 3.2 does not improve the results. Wave height dissipation is significantly reduced in Figure 4.11 due to the conservative treatment of the convective fluxes in § 2.3.3.

4.3. Wave impact on a fixed wall

Using the method described in Section 3.3, a breaking wave can be simulated without the need for a large domain for the wave to build up steepness from an initial condition (see Figure 4.12). This method for generating a periodic wave was based on the numerical experiments by Plumerault et al. (2012). The numerical methods in both the present and the reference study are based on the same treatment of the density as in Eq. (2.6). The difference between the two methods lies in the temporal discretisation of the fluid equations and the VoF interface reconstruction. Apart from these differences, the similarities between the methods in terms of solving the multi-fluid model should lead to similar results for pressure wave propagation.

4.3.1. Numerical setup

The numerical experiment as depicted in Figure 4.12 is divided into two stages:

1. An unstably steep third-order Stokes wave (§ 3.1.3) is initialised and propagated through the use of periodic boundary conditions.
2. The periodic boundary conditions are replaced by solid walls and the wave breaks against the boundary.

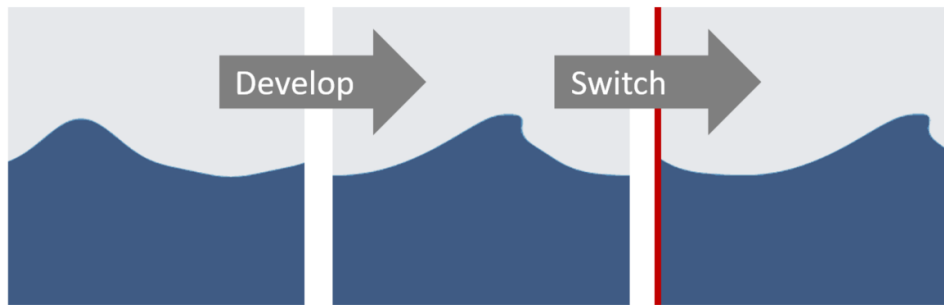


Figure 4.12: Visual description of the breaking wave experiment.

To compare wall impact for different aeration levels, the initial condition in the domain with walls should be similar. Suddenly switching boundary conditions from periodic to solid wall results in pressure waves of similar magnitude as those after impact. This is to be expected, because dropping a solid stationary wall inside a moving wave could be interpreted as an impact itself. While in the reference it is not clear what the exact steps were to initialise the wave and switch the boundary conditions, the following steps were used here:

1. The wave inflow method from Section 3.2 is used over the full width of the domain to find an initial velocity field.
2. Vertical velocity and free surface elevation are averaged horizontally so that they are positioned in the middle of each column of cells.
3. One initial iteration is performed with the incompressible solver to obtain a divergence free velocity field and an initial pressure field.
4. The wave propagates under periodic boundary conditions (stage 1) using the same incompressible solver, until the wave front is vertical.
5. This intermediate solution is saved and is used as initial condition for the second stage, where the boundaries become solid walls.
6. The solution is shifted horizontally to position the wave front at a certain distance from the wall.
7. One initial iteration and a few incompressible time steps are performed to resolve the high pressure region caused by the deceleration of the flow at the wall.
8. The obtained solution is used as input for the impact simulation (stage 2) with the compressible solver for different aeration levels.

The assumption that aeration level does not influence the initial propagation, is based on results of Plumerault et al. (2012). The same was observed when performing the experiment with the present method.

The numerical domain is a square with the size of the wavelength $\lambda = 10$ m, where the still water level is assumed to be at $y = 5$ m. The steepness of the wave is $ka = 0.55$ and the resulting wave period is $T = 2.2175$ s. The viscosity of both water and air are set to zero, because the reference experiment makes no mention of it and it is not assumed relevant for the inertia-dominated dynamics in the current case. The dimensionless simulation time t/T relative to the wave period is used in for the description and analysis in the rest of this section.

4.3.2. Impact dynamics

The wave that was generated is best described as a flip-through impact (Mai et al., 2019b) (Bredmose et al., 2010). Figure 4.13 shows some snapshots leading up to the impact, where the free-surface

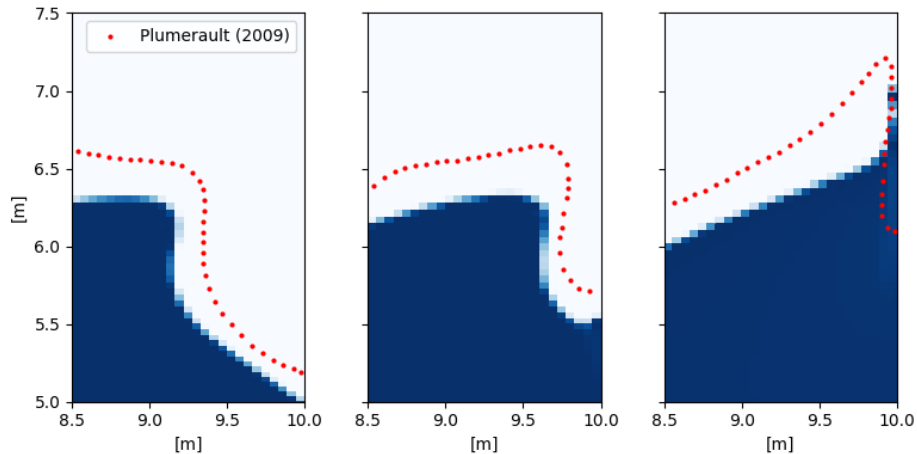


Figure 4.13: Snapshots of free-surface leading up to impact for $t/T=0.27, 0.31, 0.35$ (different times in reference free-surface, but similar $\Delta t/T$).

profile of the wave generated by Plumerault (2009) is also included to show the difference. The profiles were found almost independent of aeration level, so only the wave for the highest aeration level (5%) is shown.

No air pocket was captured by the breaking wave in the current results, which makes a comparison of air pocket oscillation frequencies and magnitude impossible. Other phenomena such as the force on the wall, pressure wave propagation, vertical pressure gradients and flow Mach numbers were still captured and will be reported in this order. The simulations have been performed on two different grids: One with square grid cells and one with vertically stretched grid cells so that a higher vertical cell resolution is obtained around the still water level. The ratio between the smallest and largest vertical cell size is 3 to 1, and the cell spacing is then defined according to Section D.2. For both grids the results turned out to be very similar, so in the coming analysis the stretched grid results are used.

Force on the wall

The forces on the wall are reported in Figure 4.14 for different aeration levels. As was expected from other literature and observations, higher aeration level impacts are characterised by a lower peak forces. The rise time also seems to be longer, but this might also be due to slightly different breaking of the wave before impact. When the maximum effort on the wall is compared to (Plumerault, 2009), the absolute percentual differences ($\|F_{\text{ref}} - F\|/F_{\text{ref}} \cdot 100\%$) are 0.7%, 1.4% and 1.5% for aeration levels 0.1%, 1.0% and 5.0%, respectively.

Pressure on the wall

The pressure on the wall over time is visualised using a spatio-temporal plot in Figure 4.15a. The slope downwards from the high pressure region after impact in Figure 4.15 shows the propagation speed of the pressure waves along the wall. The slope of this region in compares well across both figures, indicating that the methods solve propagating pressure waves in a similar way as expected.

Bullock et al. (2007) observed that for low-aeration wave impacts (defined by them as below 5.0% aeration), the pressure peak is very much localised in space and time. This type of wave impact is also characterised by little to no air entrapment, which corresponds to the observations in Figure 4.13. The distribution of dimensionless pressure on the vertical wall in Figure 4.16 fits this category quite well, see also (Bullock et al., 2007, Fig. 12a). In Figure 4.16 a dimensionless peak pressure of $p/\rho gH = 7.7$ at dimensionless altitude $y/H = 1.2$, where $H = 5$ m is the still water level. This dimensionless data is almost perfectly centered in (Bullock et al., 2007, Fig. 14), where a large data set of physical

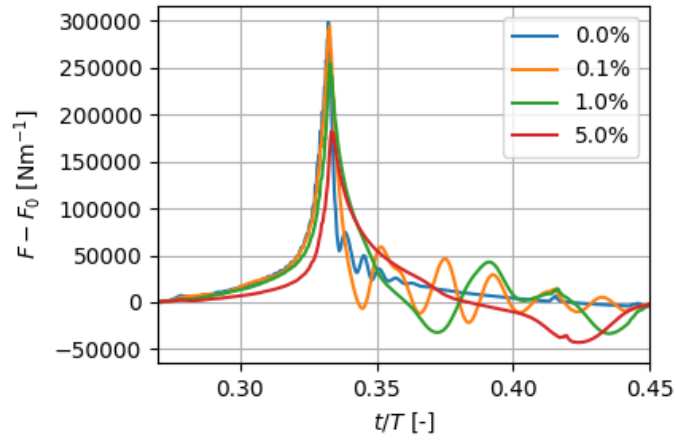
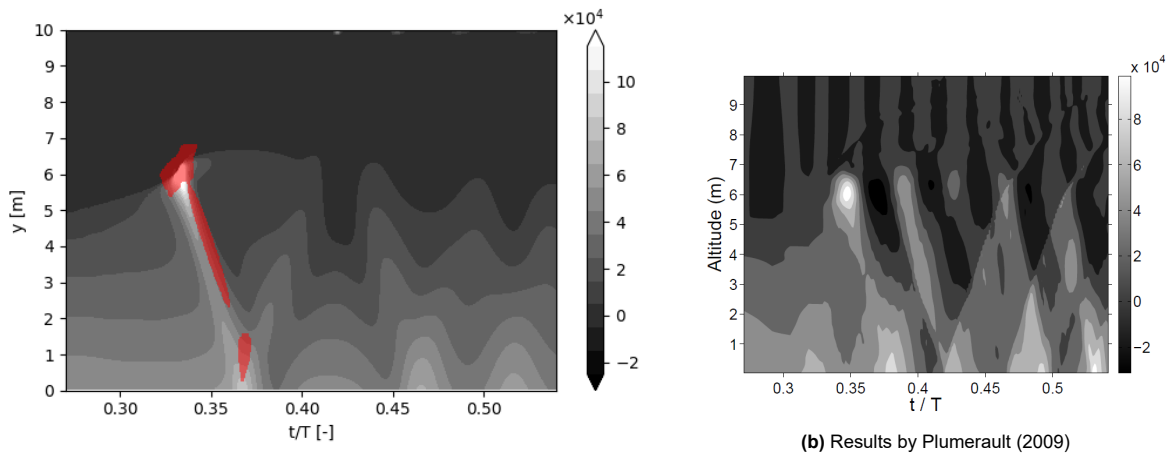


Figure 4.14: Additional total effort on the wall per meter depth, relative to quasi-hydrostatic effort $F_0 = 1.15 \cdot 10^6 \text{ N m}^{-1}$.



(a) Highlighted (red) areas where pressure gradient is large enough to lift a concrete block of 1 m.

Figure 4.15: Spatio-temporal evolution of $p - p_0$ at the wall for 5.0% aeration.

experiments of similar scale is reported.

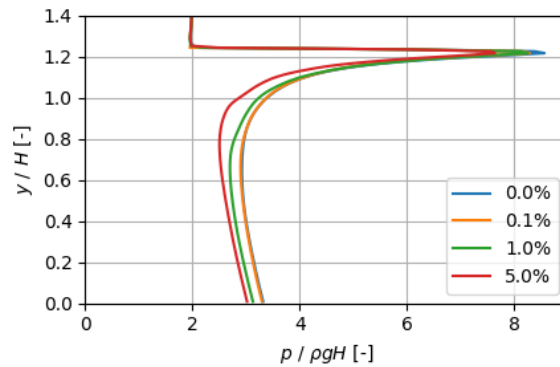


Figure 4.16: Spatial distribution of dimensionless pressure on the vertical wall at $t = t(p_{max})$.

Bredmose et al. (2010) describes this type of wave as a flip-through impact and presents results of a physical experiment without air entrainment. A peak pressure of $21\rho gH$ is observed during the experiment, which is higher than the peak pressure for the current zero aeration results. The peak pressures recorded in the current simulations stay close to $8\rho gH$ for all aeration levels. This constant peak pressure height for different aeration levels was also found in (Plumerault, 2009).

4.3.3. Pressure waves

Because the speed of sound is reduced in an aerated water mixture, propagating pressure waves are spread out in time and space. The downward propagating pressure waves in Figure 4.15a increase the intensity of pressure dynamics at the foot of the structure in Figure 4.17. The intensity of the oscillations approximately doubles if the amount of aeration is increased from 0.1% to 1.0%.

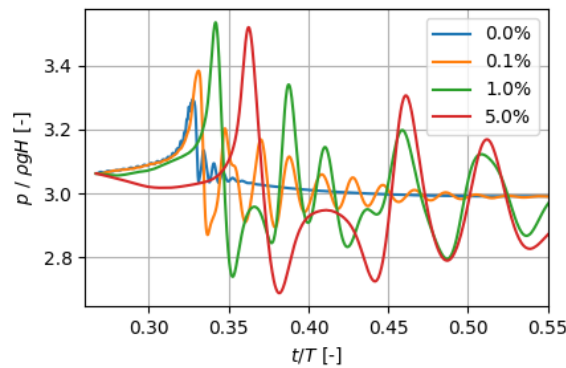


Figure 4.17: Dimensionless pressure history at the foot of the structure (lower right corner of the domain) for different aeration levels.

Due to these pressure waves propagating along the wall downwards from the impact zone, highly negative vertical pressure gradients can be found far below the surface. Such pressure gradients could cause lifting forces on submerged and sinking objects. Plumerault (2009) evaluated these vertical pressure gradients by comparing their value to a hydrostatic balance with the density of a concrete block:

$$\Delta p \geq \rho_b g \Delta z$$

For a density of concrete $\rho_b = 2500 \text{ kg m}^{-3}$, the vertical pressure gradient $\Delta p / \Delta z$ has to be below $-\rho_b g = -2.45 \cdot 10^4 \text{ Pa m}^{-1}$ to possibly move a concrete block in upward direction. In the reference (Plumerault, 2009), it was found that this threshold is easily reached for any aeration level very locally at the location and time of impact. At the peaks of subsequent oscillations of the captured air pocket, the threshold was also reached. More interestingly for the current case without air pocket, these large gradients were also found to propagate far below the surface for higher aeration levels. The results obtained with the new method show similar gradients far below the surface.

To study these vertical gradients, a moving average of the pressure gradient has been computed along the vertical wall. The height of the moving average can give an indication of the size of objects that could be displaced. In this analysis, a moving average over 1.0 m is taken along the wall. The areas on the wall where the moving average surpasses the threshold are highlighted in red on Figure 4.15a. Only for the two highest aeration levels (1.0% and 5.0%) these pressure-gradient conditions are met. In the lowest and zero aeration levels the pressure waves propagate too fast for any large gradients to persist. Although this is a very much simplified model compared to the real world, it gives an indication of the forces that could occur due to pressure waves in aerated water.

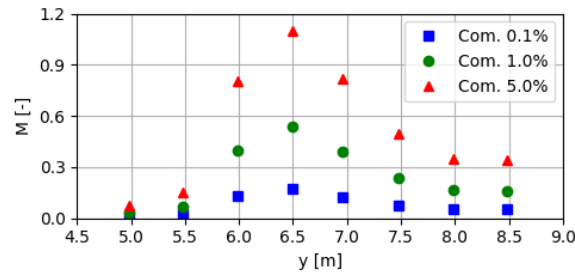


Figure 4.18: Highest recorded vertical flow Mach numbers at different altitudes and aeration levels.

4.3.4. Flow velocities

The highest recorded vertical flow velocity along the wall is similar for all aeration levels. This high velocity occurs in the vertical jet after the flip-through impact and has a magnitude of approximately 60 m s^{-1} . A flow characterised by Mach number higher than 0.3 can not be assumed incompressible anymore. To study the Mach numbers reached in the vertical jet along the wall, Figure 4.18 contains the highest recorded velocities at the wall divided by the speed of sound at the corresponding aeration level. The time at which these velocities occur differs per data point, but from time-serie data it was clear that they all occurred quickly after impact. Flow Mach numbers of above 0.3 are reached in the impact region at $y = 6.0 \text{ m}$, and even higher Mach numbers in the accelerating jet above the impact region. This shows that compressibility effects in wave impacts should not always be neglected.

4.3.5. Conclusion

Using periodic boundary conditions to develop a breaking wave, the impact dynamics on a vertical wall were studied. The simulated wave can best be described as a flip-through wave without air capture, since the flow along the wall rises upward before the wave front hits the wall. The following observations were done:

- The maximum force on the wall decreases with increasing aeration level in Figure 4.14. The reduction of peak pressure is less significant in Figure 4.16.
- The pressure wave that moves downwards along the wall propagates with the same speed as in the reference, indicating that the physical modeling of the speed of sound is indeed similar as expected. Due to these pressure waves, high vertical pressure gradients were found strong enough to lift a concrete block.
- The pressure history in Figure 4.15 and the spatial distribution in Figure 4.16 on the wall show a very local pressure peak, both in time and space. This corresponds to other literature reporting on this type of wave impact. The magnitude and location of the pressure peak for 5% aeration compares very well to experimental data of similar aeration level (Bullock et al., 2007).
- The vertical velocities in the jet along the wall after impact can reach Mach numbers over 0.3, which shows that compressibility effects in wave impacts should not be neglected.

4.4. Conclusion

This chapter reported three numerical experiments for the verification and validation of the method and the new additions. With regard to the new monolithic coupling method for rigid body interaction in Section 2.4, the following conclusion is drawn:

- Cylinder slamming with impact velocities V_{im} between 1.8 and 3.7 m s^{-1} was verified and validated against reference experiments in Figure 4.4. Buoyancy oscillations after impact compare

reasonably well to the reference results.

With regard to the implementation of wave generating boundary conditions in Chapter 3, the following conclusions are drawn:

- The wave inflow conditions of Section 3.2 were verified by simulating a regular propagating wave in long domain and comparing to analytical and reference numerical results in Figure 4.10.
- Wave height dissipation was significantly reduced by using the conservative treatment of the momentum fluxes described in § 2.3.3.
- The single periodic wave method of Section 3.3 was successfully applied to the simulation of a breaking wave impact on a vertical wall in Section 4.3. The numerical setup was clearly described in § 4.3.1 and allows for good comparison of the impact for different aeration levels.

For cylinder slamming in Section 4.1 and the breaking wave in Section 4.3, the effects of aeration on hydrodynamic impacts were investigated. In this regard, the following conclusions are drawn:

- For a cylinder entry Mach number $M_{ce} = 0.074$ the impact force is reduced by 19% in Figure 4.6b due to the compressibility of aerated water with a void fraction of $\beta = 0.05$.
- The motion of the cylinder after impact is affected mostly by the reduced density of the aerated mixture, not by the compressibility.
- During aerated flip-through wave impact on a wall, the maximum force decreases with increasing aeration level in Figure 4.14. The reduction of peak pressure is less significant in Figure 4.16.
- The reduced speed of sound in aerated water causes pressure waves that are reflected by domain boundaries in Figure 4.7 and Figure 4.17. High pressure gradients that are strong enough to lift a concrete block of 1.0 m can be found due to such pressure waves in Figure 4.15a.
- Flow velocities with Mach numbers higher than 0.3 were recorded during aerated breaking wave impact, which shows that compressibility should not be neglected.

The next chapter concerns a numerical experiment of wave impact on a pendulum, where some additional extensions to the method were required.

5

Wave impact on a pendulum

A final case study has been performed that incorporates both irregular wave generation and fluid-structure interaction. The case is based on a very recent unpublished experiment by Bos and Wellens (2021) where a focused wave hits a pendulum from standstill. It deserves its own chapter, because an additional extension had to be made for the monolithic coupling of pendulum motion in Section 5.1. The numerical setup will be described after that in Section 5.2. Generating the focused wave to hit the pendulum is described in Section 5.3. The results of the pendulum impact are presented in Section 5.4, followed by the conclusions of this chapter in Section 5.5. Finally, Section 5.6 contains a discussion on the results of this chapter.

The reference experiment and the reasons for simulating it are briefly introduced here first. A schematic overview of the reference experiment is shown in Figure 5.1. This experiment is designed to be a benchmark case for fluid-structure interaction methods in free surface waves (Bos and Wellens, 2021). The damped pendulum and free surface waves resemble the physical model of a ship that is subject to inertia, damping and restoring forces during water entry and exit. During the execution of the experiments, it was observed by the authors of (Bos and Wellens, 2021) that breaking sometimes caused aeration in the wave crest before hitting the pendulum. The reason for performing a simulation of this experiment is twofold:

- The experiment is considered an advanced benchmark case for the objectives of this thesis.
- Aeration effects may be relevant during the impact on the pendulum.

5.1. Monolithic coupling for pendulum motion

This section describes the how the motion of the pendulum is modeled. A similar method as in Section 2.4 is applied to the motion of a pendulum with length ℓ , inertia I , damping c and restoring coefficient k . The equation of motion for the angular displacement θ of the pendulum is:

$$I\ddot{\theta} + c\dot{\theta} + k \sin \theta = M. \quad (5.1)$$

Here M is an external moment exerted by the fluid on the pendulum bob. The equation of motion is discretised in time as:

$$I \frac{\dot{\theta}^{n+1} - \dot{\theta}^n}{\delta t} + c\dot{\theta}^n + k \sin \theta^{n+1} = M^{n+1}, \quad (5.2)$$

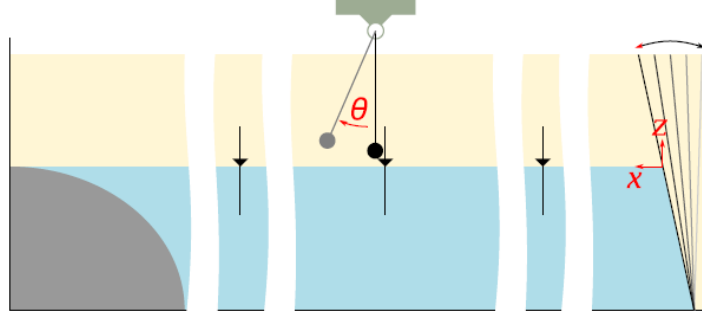


Figure 5.1: Schematic overview of the experimental setup (Bos and Wellens, 2021).

where position θ^{n+1} is already known from the explicit displacement of the body, and M^{n+1} contains the implicit part of the pressure force. Under the assumption that \mathbf{u}_b and \mathbf{f}_b are always in the same direction $\hat{\boldsymbol{\theta}}$ as the instantaneous angular motion, the following relationships are identified:

$$\dot{\theta} = \frac{\|\mathbf{u}_b\|}{\ell} = \frac{\hat{\boldsymbol{\theta}} \cdot \mathbf{u}_b}{\ell} \quad (5.3)$$

$$M = \ell \|\mathbf{f}_b\| = \ell \hat{\boldsymbol{\theta}} \cdot \mathbf{f}_b \quad (5.4)$$

Substitute the above two equations into Eq. (5.2) to obtain:

$$\frac{I \hat{\boldsymbol{\theta}}^{n+1} \cdot \mathbf{u}_b^{n+1} - \hat{\boldsymbol{\theta}}^n \cdot \mathbf{u}_b^n}{\delta t} + \frac{c}{\ell} \hat{\boldsymbol{\theta}}^n \cdot \mathbf{u}_b^n + k \sin \theta^{n+1} = \ell \hat{\boldsymbol{\theta}}^{n+1} \cdot \mathbf{f}_b^{n+1}. \quad (5.5)$$

This is then rewritten to the form of a velocity update for the absolute velocity of the pendulum bob:

$$\begin{aligned} \hat{\boldsymbol{\theta}}^{n+1} \cdot \mathbf{u}_b^{n+1} &= \hat{\boldsymbol{\theta}}^n \cdot \mathbf{u}_b^n + \delta t I^{-1} \left[\ell^2 \hat{\boldsymbol{\theta}}^{n+1} \cdot \mathbf{f}_b^{n+1} - c \hat{\boldsymbol{\theta}}^n \cdot \mathbf{u}_b^n + k \ell \sin \theta^{n+1} \right] \\ &= \hat{\boldsymbol{\theta}}^n \cdot \mathbf{u}_b^n + \delta t I^{-1} \left[\ell^2 \hat{\boldsymbol{\theta}}^{n+1} \cdot \mathbf{A}_f^{n+1} p^{n-\frac{1}{2}} - c \hat{\boldsymbol{\theta}}^n \cdot \mathbf{u}_b^n + k \ell \sin \theta^{n+1} \right] \\ &\quad + \delta t I^{-1} \ell^2 \hat{\boldsymbol{\theta}}^{n+1} \cdot \mathbf{A}_f^{n+1} \delta p^{n+1} \end{aligned} \quad (5.6)$$

Note that gravity is not included in \mathbf{f}_b here, because it is already included in the restoring coefficient k . The velocity update equation above is still only in the angular dimension and \mathbf{u}_b can still be in any arbitrary direction, which would not make sense according to the assumption made earlier. To enforce that \mathbf{u}_b is always in the direction of $\hat{\boldsymbol{\theta}}$, an equation similar to Eq. (2.28) is used to find the restricted velocity $\tilde{\mathbf{u}}_b^{n+1}$ as:

$$\tilde{\mathbf{u}}_b^{n+1} = \left(\hat{\boldsymbol{\theta}}^{n+1} \cdot \mathbf{u}_b^{n+1} \right) \hat{\boldsymbol{\theta}}^{n+1} = \begin{bmatrix} \hat{\theta}_x^2 & \hat{\theta}_x \hat{\theta}_y \\ \hat{\theta}_y \hat{\theta}_x & \hat{\theta}_y^2 \end{bmatrix}^{n+1} \begin{bmatrix} u_{b,x} \\ u_{b,y} \end{bmatrix}^{n+1} = \mathbf{T}_\theta^{n+1} \mathbf{u}_b^{n+1} \quad (5.7)$$

The final cartesian velocity update is then found by substituting Eq. (5.6) into the above:

$$\begin{aligned} \tilde{\mathbf{u}}_b^{n+1} &= \tilde{\mathbf{u}}_b^* + \delta t I^{-1} \ell^2 \left(\hat{\boldsymbol{\theta}}^{n+1} \cdot \mathbf{A}_f^{n+1} \delta p^{n+1} \right) \hat{\boldsymbol{\theta}}^{n+1} \\ &= \tilde{\mathbf{u}}_b^* + \delta t I^{-1} \ell^2 \mathbf{T}_\theta^{n+1} \mathbf{A}_f^{n+1} \delta p^{n+1} \end{aligned} \quad (5.8)$$

Here $\tilde{\mathbf{u}}_b^*$ contains all the terms that are known:

$$\tilde{\mathbf{u}}_b^* = \left(\hat{\boldsymbol{\theta}}^n \cdot \mathbf{u}_b^n \right) \hat{\boldsymbol{\theta}}^{n+1} + \delta t I^{-1} \left[\ell^2 \hat{\boldsymbol{\theta}}^{n+1} \cdot \mathbf{A}_f^{n+1} p^{n-\frac{1}{2}} - c \hat{\boldsymbol{\theta}}^n \cdot \mathbf{u}_b^n + k \ell \sin \theta^{n+1} \right] \hat{\boldsymbol{\theta}}^{n+1} \quad (5.9)$$

This velocity update is by definition always in the direction of the swinging pendulum motion at the position θ^{n+1} . For completeness, the adapted form of Eq. (2.27) is shown below:

$$\left[\begin{array}{c|c} A & Q_b \\ \hline \delta t I^{-1} \ell^2 T_\theta^{n+1} A_f^{n+1} & -I \end{array} \right] \begin{bmatrix} \delta p \\ \tilde{\mathbf{u}}_b^{n+1} \end{bmatrix} = \begin{bmatrix} \mathbf{q} \\ -\tilde{\mathbf{u}}_b^* \end{bmatrix} \quad (5.10)$$

5.2. Numerical setup

The pendulum bob in the 3D experiment is a 1.5 m long tube with a diameter of 50[mm] that fills the width of the tank, which accommodates the 2D assumption that is made here. An advantage of the cylinder is that it does not change shape when rotated, making it suitable for the translation-only solid body displacement of this method. The tube is suspended from the fulcrum with 1050 mm long aluminium profiles.

The region where the tube is expected to swing is discretised with a little over 6 *cells per diameter*. This is a very rough representation of the cylinder, which is due to the large size of the full numerical domain. The simulation was performed once without aeration and once with an initial aeration level of 1%. The density of water and air are $\rho_{\text{water}} = 1000 \text{ kg m}^{-3}$ and $\rho_{\text{air}} = 1.2 \text{ kg m}^{-3}$. Both fluids are assumed inviscid. The body is displaced with an unsplit scheme to reduce simulation time compared to the COSMIC scheme. A change of body mass over time is expected due to this setting, but this was accepted considering that a constant angular restoring coefficient k is used instead of the calculated mass.

5.2.1. Free vibration test

In this subsection In the 2D simulation the force on the object is a force per meter depth, while the pendulum tube is 1.5 m long in the experiment. To use the 2D fluid forces to excite the pendulum in the same equation of motion as derived in the experiment, these forces are multiplied by 1.5 m. The equation of motion is then written as:

$$I\ddot{\theta} + c\dot{\theta} + k \sin \theta = 1.5M_{2D}$$

The parameters I , c and k were determined from a free vibration test before the experiment (Bos and Wellens, 2021). The values that were found for these parameters are inserted in this equation to obtain:

$$\frac{2.17 [\text{kg m}^2]}{1.5 [\text{m}]} \ddot{\theta} + \frac{0.205 [\text{N m s rad}^{-1}]}{1.5 [\text{m}]} \dot{\theta} + \frac{31.7 [\text{N m}]}{1.5 [\text{m}]} \sin \theta = M_{2D} \quad (5.11)$$

Note that the parameters are divided by 1.5 m, so that the 2D fluid force can be used directly. To verify that the 2D coupling fluid-body coupling with these parameters leads to the same pendulum motion, a numerical free vibration test is performed in Figure 5.2. The quicker dissipation of energy is thought to come from additional added mass and pressure drag that add to the damping coefficient c via the interaction M in Eq. (5.11).

5.2.2. The numerical wave tank

It is not feasible for the current method to model the entire 30 m wave tank from the experiment, while also ensuring enough resolution the pendulum bob. The length of the numerical domain is set as the

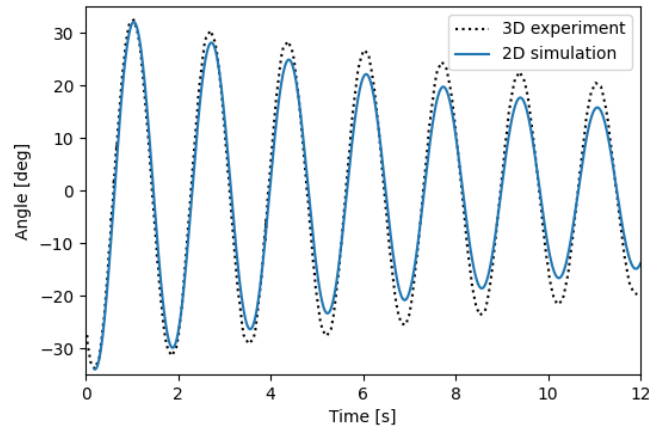


Figure 5.2: Free vibration test in air.

distance between the outermost gauges, which is 8.817 m. The pendulum is positioned 4.031 m after the first wave gauge. Figure 5.3 shows the size of the domain and gives an indication of the scale of the cylinder relative to the domain. The dots are the size of the pendulum bob at the starting location (left) and at a 12 degree angular deflection (right), which is expected to be above the maximum deflection based on the experimental results. It can be observed that the structured grid cells increase in size towards the outer boundaries, which is done according to the detailed grid stretching described in Section D.2. Table 5.1 shows the values that were used to make up the grid. The smallest cell size of 7.3 mm is found in the region of square grid cells inside the bounds around the pendulum. The largest horizontal cell size is 260 mm at the right size of the domain.

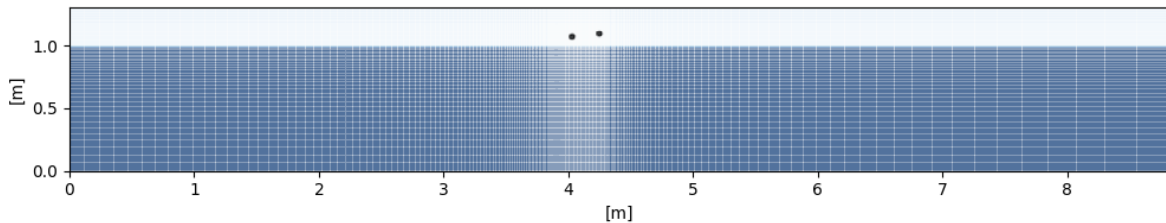


Figure 5.3: Image of the numerical wave tank used for the case study (approx. 12000 cells).

	Bounds	Cells in bound	Stretch	Total cells
X	3.981-4.279 m	41	3% / 6%	199
Y	1.039-1.122 m	11	6% / 6%	62
		451		12338

Table 5.1: Stretched grid parameters for numerical wave tank in case study.

The left boundary in Figure 5.3 is the inflow boundary corresponding to the rightmost wave gauge in Figure 5.1. Note that the x -axis has been mirrored in those figures. The bottom and rightmost boundaries are closed and a free-slip boundary condition is applied. At the top boundary the atmospheric pressure $p_{\text{atm}} = 10^5$ Pa is prescribed. The superposition of linear wave components and the closed outflow boundary will be discussed in the next section.

5.3. Irregular focused wave

This section describes the process of numerically reproducing an irregular wave from experimental measurements. The physical free surface wave in question was designed to be focused at the pendulum, so that a local steep or breaking wave hits the pendulum from standstill. The experimental measurements were taken at the wave gauges as displayed in Figure 5.1. Only the measured information at the inflow boundary (Figure 5.4) is used to determine a set of linear components using Fourier analysis.

5.3.1. Fourier analysis for wave components

Fourier analysis is applied on the time series between the red lines in Figure 5.4. This interval is chosen close around the time of interest, which is a little after the highest visible wave height. Before the interval there is very little wave action, so it is not considered very relevant for the Fourier analysis. After the interval a lot of small oscillations are visible, which are also not considered in the Fourier analysis. It is assumed that the dominant linear wave components can all be extracted from this relatively short interval. The start and end time of the interval (50.072-70.058 s) are chosen such that the wave height

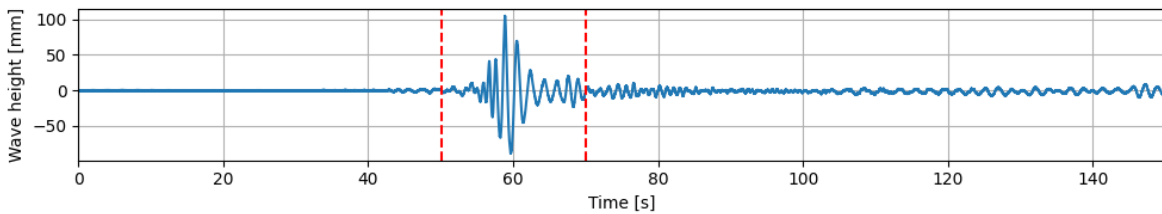


Figure 5.4: Experimental measured wave height at the inflow wave gauge.

is close to zero at these times. This is favorable for computing the discrete Fourier Transform, which is done using the `numpy.fft` module from NumPy (Harris et al., 2020). Extra care was taken to make sure that the correct phase differences were extracted according to the definition of the cosine in the linear wave definition in Eq. (3.4). Just enough frequency components were selected so that the shortest oscillations in the interval could be reconstructed. Any higher frequencies were discarded. For a table of the linear wave components that were used see Table F.1.

5.3.2. Reflection at closed boundary

No type of absorbing boundary condition has been implemented in this method yet. It was briefly considered to implement a Sommerfeld condition to prevent a lot of reflection from the outflow wall. Before implementing such a condition, a first attempt was made by running simulations with the determined wave components and a closed boundary. Keeping all other settings constant, only the length of the domain was changed for different simulations to study the influence of the wall. The simulation was started from standstill with $t = 0$ s being the beginning of the interval in Figure 5.4.

In these simulations the horizontal cell spacing was kept constant at 25 mm up to the wave gauge at the pendulum, which is left out of the simulation. After this wave gauge, the horizontal grid size was increased with 3% for each consequent cell. This was done both to decrease the total amount of cells needed, and also to use the larger grid cells at the end of the domain to dissipate some of the wave motion. Whether these larger cells did actually cause more dissipation has not been investigated.

The simulated wave heights compare reasonably well to the measurements, see Figure 5.5. The total simulation time was 15.0 s from the start of the interval in Figure 5.4, and the highest wave at the pendulum is clearly observed at just after $t = 12$ s. The results are shown from $t = 7.5$ s, to allow

zooming in at the point of interest. In the wave height signal at the inflow (top of Figure 5.5), the results

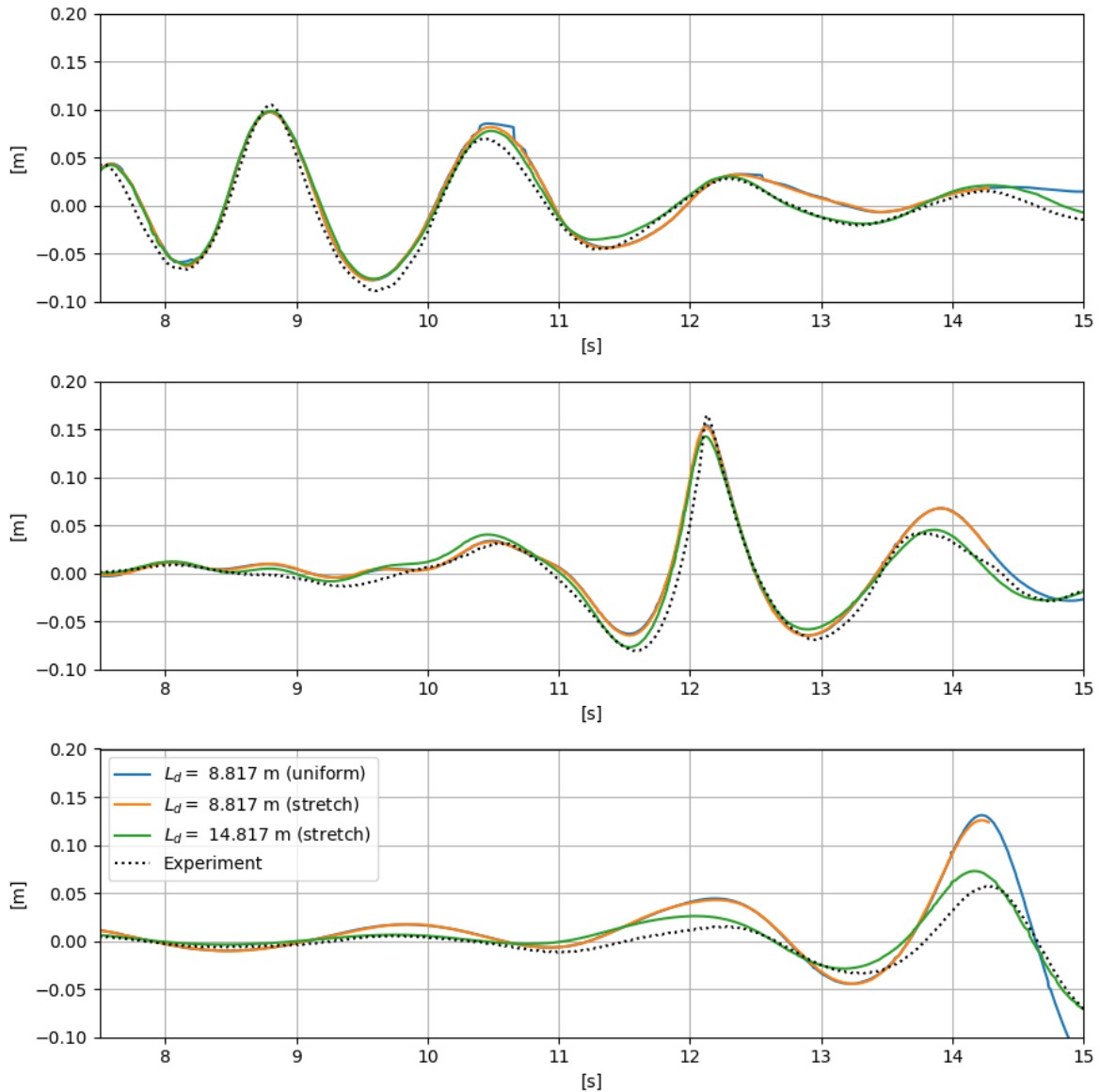


Figure 5.5: Wave heights compared to experimental measurements for different domain lengths at the inflow (top), pendulum (middle), and final wave meter (bottom).

for different domain lengths are almost identical. This is expected, as the inflow conditions are exactly the same for each simulation. It is only towards the end of the simulation that they start to differ more from each other, which could indicate an influence of the outflow boundary. The relative differences in maximum wave height at the pendulum (middle of Figure 5.5) are around 10%, suggesting that there is definitely an influence of the closed wall. At the wave gauge positioned at the outflow (bottom of Figure 5.5) of the shortest domain, the influence of reflection is clearly visible towards the end of the simulation. This is when the wave front of the large wave reaches the wall.

5.4. Impact on pendulum

The simulation including the pendulum is done using the numerical set up as described in Section 5.2. The angular deflection of the pendulum over time in Figure 5.6 compares well to the experimental

measurement. Three things can be noticed from looking at this figure: The initial acceleration, the maximum angular deflection and the oscillation period and amplitude.

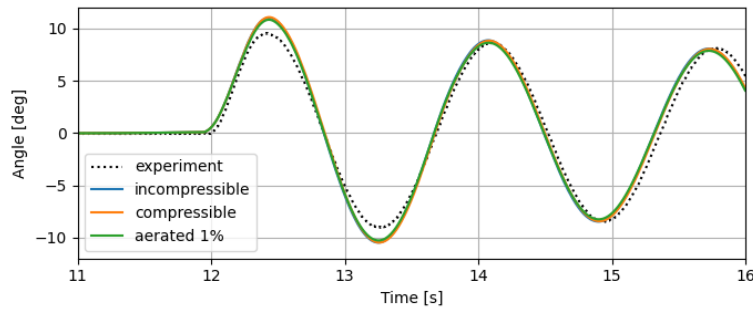


Figure 5.6: Angular deflection over time compared to the experiment.

The initial acceleration from standstill happens at almost the exact same time when comparing the simulations to the experiment. No additional operations have been performed to set the time axes equal, so this is only a result of the Fourier analysis that was performed in Section 5.3 and the fluid-structure interaction of the body during water entry. The accurate prediction of the timing of the high wave was already shown in Figure 5.5. The accurate prediction of the initial angular acceleration of the pendulum shows that the method is able to properly deal with fluid-structure interaction during water entry in a wave. For visual snapshots of the water entry and exit see Figure F.1 in Appendix F.

The simulated maximum deflection is approximately 10% higher than the experimental value. Because of the relatively coarse grid that was used during this simulation, no strong conclusions can be drawn from this difference in maximum value. However, it is expected that the simulated maximum deflection is found higher than the experimental value, due to the approximation of fully 2D fluid motion compared to the 3D experiment.

The first oscillation period is approximately the same, but then the oscillation period seems to decrease slightly. This was not observed during the free vibration test in Figure 5.2. The results are likely influenced by a second wave crest hitting the pendulum between 13.6 s and 14.0 s, altering the swinging motion of the pendulum. The amplitude decay in the second oscillation is likely also influenced by the pendulum hitting the second wave.

The simulation was done with two solvers and two aeration levels: The incompressible solver, the compressible solver with 0% aeration and the compressible solver with 1% aeration. The speed of the wave front hitting the pendulum is approximately 0.8 m s^{-1} , while the speed of sound in 1% aeration is 111 m s^{-1} . From this a cylinder entry velocity Mach number $M_{ce} < 0.01$ is found according to Eq. (4.1). Already by the conclusions of Section 4.1, we expect no significant effects due to aeration. The initial aeration level did not have a significant effect on the wave propagation, as was already expected from the results in Section 4.3 and of (Plumerault, 2009).

5.5. Conclusion

In this chapter the monolithic coupling method of Section 2.4 was extended to the motion of a pendulum, which was verified by a free vibration test in Figure 5.2. By decomposing an experimental wave height signal into a superposition of linear wave components using Fourier analysis, a steep focused wave was generated.

- The time history of the wave height measured at the pendulum could be reproduced reasonably well in Figure 5.5.

- The initial acceleration due to impact and maximum deflection of the pendulum compare well to the experimental results in Figure 5.6.
- The impact velocity of the steep wave front against the pendulum was too low to distinguish any effect of a homogeneous initial aeration level of 1%.
- The propagation of the wave was not influenced by the initial aeration.

5.6. Discussion

The results obtained here are for a relatively coarse grid with approximately 6 *cells per diameter*. Simulations could be performed again for higher resolutions to see where the results converge to. But before this is done, it should be considered whether the current experiment is suitable for the current method. Right now the impact velocities are too low to observe any effects of aeration. If a more violently breaking aerated impact can be created in the physical basin and reproduced in the numerical wave tank, this could be used in the further validation of the present method.

Two additional numerical subjects of discussion arose from the displacement of the pendulum bob through the numerical domain. A consequence of the current implementation of the equation motion is that the center of gravity diverts from the prescribed path. A consequence of the body volume displacement with an unsplit scheme in diagonal direction is that the total volume increases. Both topics are addressed in the following subsections.

5.6.1. Swing radius of the pendulum

Due to the way the pendulum equation of motion is implemented, a discrepancy between the experimental swing radius and the numerical swing radius can arise. This difference is likely caused by the explicit displacement of the body based on the velocity in angular direction as determined from coupled pendulum motion system in Eq. (5.10). Nothing forces the new center of mass to remain at the exact pendulum trajectory, so over time the center of gravity can move outward slightly in radial direction.

The oscillatory behavior of the radius in Figure 5.7 has twice the frequency of the pendulum oscillations. At the turning points of the pendulum oscillation, the radius change is low. This could confirm the expectation that it is caused by the Forward Euler displacement scheme. The radius change is also low at the lowest swing point, where the angular velocity is highest. This indicates that it also depends on the velocity or the direction of the velocity. In the numerical free vibration test (Figure 5.2) the increase in radius was observed to be around 1% over 7 oscillation periods.

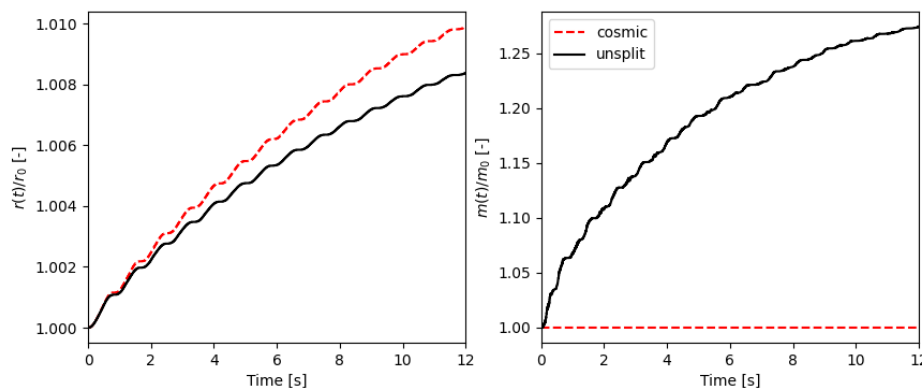


Figure 5.7: Change in radius (left) and total volume (right) of the bob compared to their initial values in the free vibration test.

5.6.2. Total volume of the pendulum bob

The mass or volume increase due to the unsplit scheme is clearly visible in the results of free vibration test (right of Figure 5.7). The cosmic scheme caused no observable volume change. Because an unsplit scheme was used to displace the body volume in the case study, it was found that the total volume increased by around 1% before the end of the simulation. As mentioned before, this consequence was accepted with the idea that the equation of motion did not consider the mass of the cylinder but only the restoring force coefficient in Eq. (5.11). Another consequence of an increased total volume is that the total surface area is likely also larger, meaning that pressures are integrated over a larger surface.

Both the increase of radius and total volume seem to decrease over time. This can likely be explained by the decreasing maximum velocities of the solid body, which decreases the proneness to displacement errors. For simulations with high pendulum bob velocity, both these effects should not be neglected. For simulations with a long duration, like in the experiment with continuous loading by monochromatic waves (Bos and Wellens, 2021), both effects could increase with time and should also be prevented.

6

Conclusion

The aim of this thesis was to evaluate the effect of aerated water impacts on rigid body dynamics. With regard to this aim, the following conclusions were drawn from the experiments in Section 4.1 and Chapter 5:

- During slamming of a buoyant cylinder with entry Mach number $M_{ce} = 0.074$, the sustained impact force is reduced by 19% in Figure 4.6b due to the compressibility of aerated water with void fraction 0.05.
- Deeper surface penetration after impact with $M_{ce} < 0.1$ in § 4.1.3 is caused by the reduced density of the aerated water mixture, not by the increased compressibility.
- For a cylinder entry Mach number of $M_{ce} \leq 0.01$ the effect of compressibility of the fluid can be neglected in Figure 4.6b and Section 5.4.

The main objective was to extend the state-of-the-art numerical method EVA for aerated water impacts with a coupling method for fluid-rigid body interaction in Chapter 2. The secondary objective was to implement wave inflow conditions for both regular and irregular waves in Chapter 3. From the experiments in Chapter 4 and Chapter 5, the following conclusions for aerated water impacts were drawn:

- The influence of the velocity of air in inflow conditions was found to be negligible during regular wave propagation in § 4.2.2.
- The maximum additional total effort on a wall due to flip-through wave impact is reduced by 35% for a void fraction $\beta = 0.05$ in Figure 4.14. The peak pressure is reduced much less in Figure 4.16.
- The very local spatial distribution of impact pressure during a flip-through wave impact is unaffected by void fractions $\beta < 0.05$ in Figure 4.16.
- The reduced speed of sound in aerated water causes upwards vertical pressure gradients more than twice as large as the hydrostatic gradient in Figure 4.15.
- The condition for incompressibility $M < 0.3$ is exceeded during flip-through wave impact with void fractions $\beta > 0.01$ in Figure 4.18.
- Pressure waves from initial impact in aerated water can double the intensity of reflected pressures in corners of impact-surrounding domains, as shown for a breaking wave in Figure 4.17 and for a cylinder impact in Figure 4.7.

It can be concluded from this thesis that the compressibility effects of aeration on penetration depth during cylinder slamming can be neglected for entry Mach numbers below 0.1. For further research, it is recommended that this numerical method is used for a range of experiments with various geometries and higher impact velocities. By continuing to enable more types of aerated water impact simulations, better decisions can be made on when to consider the full effects of aerated water on hydrodynamic impacts.

7

Discussion

This chapter contains a discussion on the results of this graduation project. First, we discuss in a more general sense the range of applicability of the findings in Section 7.1. Second, recommendations for further research are given in Section 7.2. Finally, some comments are made on the method implementations Section 7.3.

7.1. Range of applicability

The conclusions drawn from specific numerical experiments that were performed during this thesis may have more general implications in a wider range of applicability. Here some of these potential implications are discussed.

The effects of aeration in hydrodynamic impacts on rigid bodies can be considered significant when the goal is to estimate the impact loads on a marine structure. If the maximum total force on a rigid body is important for the case at hand, the cushioning effect due to aeration should be considered. An example of such a case could be a high-speed craft repeatedly slamming aerated water waves. When the local distribution of loads on the surface of a rigid body is of interest, the different temporal and spatial distribution of impact pressures in aerated water may also be significant. An example of such a case could be the load estimation for fatigue analysis of a flat plate, which is also mentioned in other literature (Mai et al., 2019a).

If only the resulting motion of a rigid body is of interest, simulation methods assuming incompressible flow may well be sufficiently accurate in some cases. One could account for aeration in the water by simply reducing the density of the incompressible fluid.

Regions surrounding an aerated water impact can also be affected. Strong pressure waves may travel away from the impact zone, affecting neighbouring structures or boundaries of closed compartments. This could become especially relevant when reflecting pressure waves excite a resonant frequency of the surrounding structure.

Something that was not thoroughly discussed in this thesis is the physical scale of an aerated water impact. The experiments during this work have been performed at the scale of the reference experiments they were compared to. It is however expected that at larger physical scale the effects due to the compressible properties of aerated water, such as cushioning, may well be more significant. This is because higher flow Mach numbers are expected when scaling is done according to Froude scaling,

for example.

The study of hydrodynamic impacts on marine structures remains a complex topic. The current state-of-the-art numerical methods have come as far as to accurately model some hydrodynamic impacts including the effect of air and aeration. By modeling the effect of air and aerated water in a continuously increasing range of realistic numerical experiments, it will become clearer where these effects should not be neglected. By gradually increasing knowledge on this topic, we can hopefully apply this in situations where aeration has important consequences for the design of ships.

7.2. Recommendations for further research

Recommendations for further research following directly from the results of this thesis are given:

- The very brief qualitative comparison of aeration effects during cylinder water impact that was included in § 4.1.3 can be extended much further. It will be interesting to see if the relationships from other numerical methods or physical experiments can be reproduced with the current method for flat water impacts. The series on cylinder impacts in aerated water can be extended to provide a non-dimensional analysis of the reduction of impact force in aerated water impacts for blunt (but not flat) bodies. It is recommended that simulations with higher impact velocities are performed, where the effect of aeration is more visible
- In Section 4.3 a flip-through type wave was generated and studied. This type of wave is actually not so common in physical environments (Plumerault, 2009) due to its ideal nature. It will be interesting to study the effects of aeration in other, more common types of breaking waves against a wall or other objects. Quite some literature exists on different types of wave impacts (Section A.1), so comparison material is available.

Other, less directly related topics of interest are identified below:

- No still floating objects have been simulated, it can be interesting to know whether a steady state can be reached in the way the method is currently set up. Especially objects with sharp corners are an interesting topic in this regard due to the surface reconstruction in those corner regions.
- Implementation of absorbing boundary conditions, such as in (Wellens, 2012), might extend the possible use-cases for this method. In this thesis, a specific selection of experiments eliminated the need for these boundary conditions. However, many other cases relevant to the marine industry may require a method for open boundaries.

7.3. Comments on method implementations

During the writing of this thesis and the numerical experiments that were performed, the code that makes it all possible was under constant development. While the settings that have been used for each numerical experiment have been documented, some results might still suffer from small mistakes that have gone unnoticed. As a consequence, reperforming the experiments with a future version of the code is not guaranteed to give the exact same outcome. But as time progresses, one can hopefully assume that different results mean better results.

The monolithic coupling method implemented in this thesis has limited use-cases. For translational motion of rigid bodies it may be efficient to use a monolithic method as it decreases the amount of iterations performed during a time step. The gain in computational expense has not been investigated, but it might be so that a monolithic method for many degrees of freedom becomes more expensive than a partitioned iterative method.

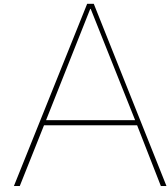
A general disadvantage of monolithic methods is that they are specific to the numerical method they are implemented in. In the current work this is accepted, but it reduces the modularity of the method. As a consequence, any changes to the fluid equations have to be considered for the body velocity update equation.

Bibliography

- Aghaei, A., Schimmels, S., Schlurmann, T., and Hildebrandt, A. (2020). Numerical investigation of the effect of aeration and hydroelasticity on impact loading and structural response for elastic plates during water entry. *Ocean Engineering*, 201.
- Bos, R. and Wellens, P. (2021). Fluid–structure interaction between a pendulum and monochromatic waves. *Journal of Fluids and Structures*, 100:103191.
- Bredmose, H., Hunt-Raby, A., Jayaratne, R., and Bullock, G. N. (2010). The ideal flip-through impact: experimental and numerical investigation. *Journal of Engineering Mathematics*, 67(1):115–136.
- Bredmose, H., Peregrine, D. H., and Bullock, G. N. (2009). Violent breaking wave impacts. part 2: modelling the effect of air. *Journal of Fluid Mechanics*, 641:389–430.
- Buchner, B. (2002). *Green water on ship-type offshore structures*. Phd thesis, Delft University of Technology.
- Bullock, G., Crawford, A., Hewson, P., Walkden, M., and Bird, P. (2001). The influence of air and scale on wave impact pressures. *Coastal Engineering*, 42(4):291–312.
- Bullock, G. N., Obhrai, C., Peregrine, D. H., and Bredmose, H. (2007). Violent breaking wave impacts. part 1: Results from large-scale regular wave tests on vertical and sloping walls. *Coastal Engineering*, 54(8):602–617.
- Crawford, A. R. (1999). *Measurement and analysis of wave loading on a full scale coastal structure*. Thesis, University of Plymouth.
- Duz, B., Borsboom, M., Wellens, P., Veldman, A., and Huijsmans, R. (2016). Efficient and accurate plic-vof techniques for numerical simulations of free surface water waves. *In Proceedings of the 9th International Conference on Computational Fluid Dynamics - ICCFD9*.
- Elhimer, M., Jacques, N., El Malki Alaoui, A., and Gabillet, C. (2017). The influence of aeration and compressibility on slamming loads during cone water entry. *Journal of Fluids and Structures*, 70:24–46.
- Facci, A. L., Falcucci, G., Agresta, A., Biscarini, C., Jannelli, E., and Ubertini, S. (2019). Fluid structure interaction of buoyant bodies with free surface flows: Computational modelling and experimental validation. *Water*, 11(5).
- FAO (2020). The state of world fisheries and aquaculture 2020. sustainability in action. Technical report, FAO.
- Fekken, G. (2004). *Numerical simulation of free-surface flow with moving rigid bodies*. Thesis.
- Gu, H. B., Causon, D. M., Mingham, C. G., and Qian, L. (2013). Development of a free surface flow solver for the simulation of wave/body interactions. *European Journal of Mechanics - B/Fluids*, 38:1–17.

- Gu, H. B., Qian, L., Causon, D. M., Mingham, C. G., and Lin, P. (2014). Numerical simulation of water impact of solid bodies with vertical and oblique entries. *Ocean Engineering*, 75:128–137.
- Harris, C. R., Millman, K. J., van der Walt, S. J., Gommers, R., Virtanen, P., Cournapeau, D., Wieser, E., Taylor, J., Berg, S., Smith, N. J., Kern, R., Picus, M., Hoyer, S., van Kerkwijk, M. H., Brett, M., Haldane, A., del Río, J. F., Wiebe, M., Peterson, P., Gérard-Marchant, P., Sheppard, K., Reddy, T., Weckesser, W., Abbasi, H., Gohlke, C., and Oliphant, T. E. (2020). Array programming with numpy. *Nature*, 585(7825):357–362.
- Hieu, P. D., Katsutoshi, T., and Ca, V. T. (2004). Numerical simulation of breaking waves using a two-phase flow model. *Applied Mathematical Modelling*, 28(11):983–1005.
- Kleefsman, K. M. T. (2005). *Water impact loading on offshore structures. - A numerical study*. Phd thesis, University of Groningen.
- Kundu, P. K., Cohen, I. M., and Dowling, D. R. (2016). Chapter 15 - compressible flow. In Kundu, P. K., Cohen, I. M., and Dowling, D. R., editors, *Fluid Mechanics (Sixth Edition)*, pages 819–879. Academic Press, Boston, sixth edition edition.
- Liu, S., Gatin, I., Obhrai, C., Ong, M. C., and Jasak, H. (2019). Cfd simulations of violent breaking wave impacts on a vertical wall using a two-phase compressible solver. *Coastal Engineering*, 154.
- Lugni, C., Brocchini, M., and Faltinsen, O. M. (2006). Wave impact loads: The role of the flip-through. *Physics of Fluids*, 18(12).
- Ma, Z. H., Causon, D. M., Qian, L., Mingham, C. G., Gu, H. B., and Ferrer, P. M. (2014). A compressible multiphase flow model for violent aerated wave impact problems. *Proceedings of the Royal Society A: Mathematical, Physical and Engineering Sciences*, 470(2172).
- Ma, Z. H., Causon, D. M., Qian, L., Mingham, C. G., Mai, T., Greaves, D., and Raby, A. (2016). Pure and aerated water entry of a flat plate. *Physics of Fluids*, 28(1).
- Mai, T., Mai, C., Raby, A., and Greaves, D. M. (2019a). Aeration effects on water-structure impacts: Part 1. drop plate impacts. *Ocean Engineering*, 193.
- Mai, T., Mai, C., Raby, A., and Greaves, D. M. (2019b). Aeration effects on water-structure impacts: Part 2. wave impacts on a truncated vertical wall. *Ocean Engineering*, 186.
- Mwasilu, F. and Jung, J.-W. (2018). Potential for power generation from ocean wave renewable energy source: a comprehensive review on state-of-the-art technology and future prospects. *IET Renewable Power Generation*, 13(3):363–375.
- Plumerault, L.-R. (2009). Numerical modelling of aerated-water wave impacts on a coastal structure.
- Plumerault, L. R., Astruc, D., and Maron, P. (2012). The influence of air on the impact of a plunging breaking wave on a vertical wall using a multifluid model. *Coastal Engineering*, 62:62–74.
- Rienecker, M. and Fenton, J. (1981). A fourier approximation method for steady water waves. *Journal of Fluid Mechanics*, 104:119–137.
- Russo, S., Biscarini, C., Facci, A. L., Falcucci, G., Jannelli, E., and Ubertini, S. (2017). Experimental assessment of buoyant cylinder impacts through high-speed image acquisition. *Journal of Marine Science and Technology*, 23(1):67–80.

- van der Eijk, M. (2018). Numerical modelling of homogeneous aerated-water wave impacts. Thesis, TU Delft.
- van der Eijk, M. and Wellens, P. R. (2019). A compressible two-phase flow model for pressure oscillations in air entrapments following green water impact events on ships. *International Shipbuilding Progress*.
- van der Eijk, M. and Wellens, P. R. (2021a). Numerical modelling of a two-dimensional extreme homogeneous aerated green water impact. *Unpublished*.
- van der Eijk, M. and Wellens, P. R. (2021b). Two-phase free-surface flows and moving bodies with an efficient momentum preserving vof cut-cell method. *Unpublished*.
- Vandamme, J., Zou, Q., and Reeve, D. E. (2011). Modeling floating object entry and exit using smoothed particle hydrodynamics. *Journal of Waterway, Port, Coastal, and Ocean Engineering*, 137(5):213–224.
- Veldman, A., Seubers, H., Hosseini Zahraei, S. M., Chang, X., Wellens, P., Plas, v. d. P., and Helder, J. (2019). The commotion project : Computational methods for moving and deforming objects in extreme waves. *Computational Methods in Marine Engineering MARINE2019*.
- Wellens, P. R. (2012). *Wave Simulation in Truncated Domains for Offshore Applications*. Thesis, Delft University of Technology.
- Wemmenhove, R. (2008). *Numerical Simulation of Two-Phase Flow in Offshore Environments*. Phd thesis, University of Groningen.
- Wemmenhove, R., Luppès, R., Veldman, A. E. P., and Bunnik, T. (2015). Numerical simulation of hydrodynamic wave loading by a compressible two-phase flow method. *Computers & Fluids*, 114:218–231.
- Wilson, P. S. and Roy, R. A. (2008). An audible demonstration of the speed of sound in bubbly liquids. *American Journal of Physics*, 76(10):975–981.
- Wood, A. (1946). *A textbook of sound*.
- Youngs, D. (1984). An interface tracking method for a 3d eulerian hydrodynamics code.
- Zhao, X., Ye, Z., Fu, Y., and Cao, F. (2014). A cip-based numerical simulation of freak wave impact on a floating body. *Ocean Engineering*, 87:50–63.
- Zuzio, D., Orazzo, A., Estivalèzes, J.-L., and Lagrange, I. (2020). A new efficient momentum preserving level-set/vof method for high density and momentum ratio incompressible two-phase flows. *Journal of Computational Physics*, 410:109342.



Literature review

This chapter contains a literature review on the topics relevant to this thesis. The three topics that are discussed are aerated water impacts in Section A.1, fluid-structure interaction in Section A.2 and wave generation in Section A.3.

A.1. Aerated water impacts

This section contains an overview of studies on the different effects of aeration on hydrodynamic impacts. Hydrodynamic impacts are commonly divided in three different sorts: Breaking wave impacts, slamming impacts and green water loading. For these three sorts of impact, a literature overview is presented in § A.1.1, § A.1.2 and § A.1.3, respectively.

A.1.1. Wave impact

Most hydrodynamic wave impact studies are performed for assessing the loads on either fixed shore breakwaters or the insides of tanks aboard ships. In the first, wave motion and breaking is induced by swell, wind and/or bottom topography, while in the latter the wave motion (sloshing) is caused by the motion of the ship. Both fields of study refer to the same types of breaking waves, so they are referred to here without considering their specific physical application.

A flip-through wave impact including air cavity is shown to cause pressure oscillations after impact due to the oscillations of the trapped air pocket. A flip-through impact where phase-mixing (aeration) occurs is heavily influenced by 3D effects and smaller and higher frequency oscillations can be observed, caused by smaller bubble sizes (Lugni et al., 2006). Aerated wave impacts on a wall are characterized by less localized pressure spikes and longer rise times (Bullock et al., 2007), and whilst the peak pressure in a less-aerated wave impact is often higher, the wider spatial distribution during an aerated impact could cause the total resultant force to be similar or higher. The total impulse of aerated impact may well be higher due to the longer duration, according to the authors. Another recent study did physical experiments of aerated water impact on a truncated vertical wall and found that high aeration impact including air pocket is among the most severe types of impact (Mai et al., 2019b). Post-impact high frequency pressure oscillations of trapped air pockets were observed, and may need to be considered in fatigue analysis of ship structures.

Numerically modeling the air as a second compressible phase is preferred for studying wave breaking and air entrapment, because the dynamics of the compressible second phase affects the fluid dis-

tribution and pressure level of the liquid phase (Wemmenhove et al., 2015). Because the free surface has to be kept sharp in violent flow conditions, a new density-averaging method is used at the free surface. A more recent study that treated air as a second compressible phase, found good agreement between numerical results and experiments of several types of breaking wave impacts (Liu et al., 2019). This paper also stresses the importance of keeping the interface sharp during violent flow conditions and they employ a Ghost Fluid Method to do so.

By also modeling the water phase as a compressible mixture of water and air, many phenomena observed by Bullock et al. (2007) during aerated impacts could be reproduced (Bredmose et al., 2009). Among the reproduced phenomena were the oscillatory pressures associated with the oscillating air pockets and pressure waves propagating through the compressible aerated water. Plumerault et al. (2012) were able to reproduce the same phenomena and found that the influence of the air pocket oscillations is dominant in the dynamic efforts on a wall. Using another numerical method, Ma et al. (2014) also reproduced the same phenomena. Their work is concluded by saying that their compressible two-phase model is favorable over incompressible solvers, but that the treatment of the free surface can diffuse the interface over several cells.

A clear definition of the interface is important when modeling two phases with different fluid properties (Plumerault, 2009). Lack of a sharp interface (e.g. an interface diffused over multiple cells) makes it hard to define mixture laws for the properties such as density, viscosity or compressibility around the contact discontinuity.

A.1.2. Slamming

Wave slamming type impacts are often studied in flat water for simplicity's sake, but these impacts only happen when a vessel undergoes extreme heaving or pitching motion. Such extreme motions occur mainly under rough conditions, where breaking waves and white capping are very common. Thus, the presence of aerated water in the ocean's surface is likely.

Experiments and numerical computations show that peak load on a slamming flat plate can be reduced by half with 1.6% aeration in water (Ma et al., 2016). The resulting impulse on the plate is not necessarily much smaller than for pure water impact. Physical experiments of cone water entry in bubbly water confirms that aeration can cause a reduction of impact force and slamming coefficient (Elhimer et al., 2017). Hydrodynamic impact pressure and force for a flat drop plate are significantly lower when measured in aerated water compared to pure water, but there is almost no reduction of the total loading impulse (Mai et al., 2019a). In a numerical study that investigated the combined effects and feedback mechanism of aeration and hydroelasticity on slamming, reduced peak load but longer load duration were again observed for only slight amounts of aeration (Aghaei et al., 2020).

A.1.3. Green water

Another extreme free surface event, which is related to wave impact, is green water loading. A green water event occurs when relative wave motions exceed the freeboard of a ship and cause water to enter on deck, which is a complex and non-linear process. To be able to simulate green water impacts fully, a numerical method should be able to deal with complex non-linear flows like water entry of a flared bow structure, flow onto the deck, the actual impact and more (Buchner, 2002).

A numerical study on green water simulation shows that wave run-up onto the deck can be simulated in three dimensions using the method ComFLOW (Kleefsman, 2005). But the low resolution required to achieve this, causes great loss of detail at the location of impact. The level of detail becomes important when simulating the dynamics of air pockets in these types of impacts. In a more recent addition to the same method, the simulation of a dam break and air pocket dynamics in two

dimensions was validated (van der Eijk and Wellens, 2019). It was found that the magnitude of the pressure oscillations in the air pocket is of the same order as the impact pressure. These authors also stress the importance of a sharp representation of the free-surface for modeling the interaction between water and air accurately.

The effect of aeration on green water loading was investigated in (van der Eijk, 2018; van der Eijk and Wellens, 2021a) using a numerical dam break experiment. Similar to other studies, it was found that initial impact pressures reduce with aeration levels from 0% to 5%. Due to the compression oscillations of an entrapped air pocket, sub-atmospheric pressures were found that caused lifting forces on an obstacle in the dam break simulation. Additionally, pressure waves were found to interact with acoustic modes between two structures, causing a pressure increase.

A.2. Fluid-structure interaction in two-phase flow methods

While many of the experiments that were mentioned in Section A.1 are relevant for the impact dynamics on marine structures, they are mostly simplifications of realistic situations. As indicated by Buchner (2002), a fully integrated (and properly validated) numerical simulation method for green water events can give great insight in velocity fields and pressure distributions. This statement is interpreted here in the broader application to all types of wave impact on marine structures, where in reality the motion of the structure interacts with the fluid. This rest of this subsection discusses some studies that have simulated fluid-structure interaction in two-phase flow models for the marine environment.

In § A.1.2, a study on flat plate slamming by Aghaei et al. (2020) was already discussed that considered both hydroelasticity and aeration. The authors found that for an aeration level of 5% and higher, the peak load is almost independent of the plate flexibility. They mention that this could imply that studies on modeling aerated breaking wave impacts may not need to use strong coupling for accurate assessment of hydroelastic impact loads.

Because of the above and to limit the scope of this study, only rigid body motion will be explored in the context of free surface flow and breaking waves. In the study on the effect of air on hydrodynamic impact loads, moving rigid bodies are relevant in cases where structure motion in waves is important, like green water loading (Buchner, 2002), floating breakwaters, drilling platforms, wave energy devices and so on (Zhao et al., 2014).

Recognizing the importance of moving bodies in many engineering applications, Gu et al. (2013) develop a two-phase free surface flow model with moving bodies. Their flow model would be extended to cases involving wave interactions with floating bodies and additionally it would be linked to flow models that accommodate aerated water. Vertical and oblique water entry of solid objects is investigated using the model and the results compare well with other experimental data (Gu et al., 2014), but interactive motion with floating bodies in aerated water is not included.

A study that included interactive body motion in wave simulations, reproduced nonlinear interaction of freak waves with a floating rigid body (Zhao et al., 2014). A qualitative and quantitative comparison to a physical experiment of a wave entering on the deck of a floating structure shows that this numerical model is capable of simulating nonlinear wave-body interaction, distorted free surfaces and strong viscous flows. While entrapped air was present in both the experiment and numerical simulations, no comments were made on the pressure dynamics inside these air pockets.

The coupling of fluid and body in that study was done by an Immersed Boundary method, imposing the effects of the solid body on the fluid as a boundary condition during time integration. The use of this type of method may smooth discontinuities over the interface, which is not preferred for convection-

dominated flows (Fekken, 2004). The importance of the contact discontinuity of the water-air interface was already highlighted in § A.1.1. A similar importance thus applies to the interface between fluids and solid geometries.

In a study on green water loading, a beginning is made with interactive motion of floating rigid bodies in one-phase free surface flow in ComFLOW (Fekken, 2004). The body boundary in the fluid is treated using cut-cells to keep the interface sharp. The force on the body is found by integrating the pressure over the boundary, while neglecting viscous friction. The numerical coupling when treating the force on the body explicitly is shown to become unstable when the added mass is larger than the solid mass, which is often the case for floating bodies. A fully implicit iterative solving routine is used to overcome this instability. The most recent addition to the method ComFLOW is a numerical coupling method that can handle large added-mass ratios efficiently for rigid bodies and elastically deforming bodies (Veldman et al., 2019). The treatment of body boundaries still uses the same type of cut-cell method.

The above-mentioned numerical methods are all Eulerian methods in terms of solving the fluid motion. A Lagrangian method called Smoothed Particle Hydrodynamics was used by Vandamme et al. (2011) to simulate floating cylinders and interactive falling wedges, where free surface profiles and interactive body motion agreed well to other experimental and numerical results. This type of method is not considered further, as there is no clear definition of a water-air interface.

A.3. Wave generation in two-phase flow methods

In this thesis, we are interested in wave generation methods for enabling more realistic simulations that include regular and irregular wave motion. Specifically, the interest is in wall inflow boundary conditions for free-surface waves and the velocity of the air above the free surface, since not much can be found on this.

Inflow conditions below the free surface are commonly defined by approximating an analytical velocity profile over the discrete grid, such as the one-phase flow boundary conditions in (Wellens, 2012). Similarly, such boundary conditions are prescribed in a related two-phase flow method in (Wemmenhove et al., 2015). Another way of generating wave in two-phase flow is by mimicking the physical wave-maker that is used in experimental wave tanks, such as in (Hieu et al., 2004). Finally, solutions from an external solver can be used to prescribe boundary conditions on the domain wall.

The studies on aerated water wave impacts discussed in § A.1.1 mostly employ one of the three methods discussed above. One exception is (Plumerault et al., 2012), which uses periodic boundary conditions to propagate a single regular wave from an initial wave velocity field to eliminate the need for wave propagation in a long numerical domain.

In the studies mentioned here, no specifications were found for the velocities of air above the free surface at inflow boundary conditions. Whether the lack of reporting on this is due to negligible effects on further propagation on waves, remains open to be answered.

A.4. Conclusion

This section shortly summarizes the previous sections in this literature review. Conclusions drawn here are used in the formulation of the research approach in Section 1.2.

In Section A.1 we gave an overview of the state of literature on three types of aerated wave impacts: Breaking waves, slamming and green water loading. Despite the difference in impact type, the physical

effects of aeration on impact dynamics are similar between them. For all three types, aeration often causes less localized and reduced peak loads that may sustain longer compared to incompressible flow impacts. The total severity of an aerated impact differs from case to case, but can be just as severe when measured in terms of total impulse. Entrapped air pockets can cause oscillations due to the compression and expansion of the compressible air. Any resulting pressure waves after impact propagate slower through aerated water and may induce strong gradients or resonant behaviour in the presence of structures.

Modeling aerated water as a compressible fluid in two-phase flow allows numerical reproduction of many physically observed phenomena. These phenomena include oscillatory pressures in entrapped air pockets and slower propagating pressure waves after impact in aerated water. It is recognized by multiple authors that a sharp interface is important to model the contact discontinuity between two phases with different properties.

While several methods exist for simulating two-phase flow including interactively moving rigid bodies, no studies were found that have included this in an aerated water model. Similar to the water-air interface, having a clear definition of the interface between water and solid geometry is important for modeling the contact discontinuity between them.

The generation of free-surface waves at the boundaries of a numerical domain with two-phase flow can be achieved by: Approximating an analytical solution, simulating a physical wave-maker, or using an external solver. Velocities of air above the free-surface are often not specified.

B

VoF fractions and labelling

This appendix provides a description of the VoF-method and displacement algorithms used for the modeling of both fluid-fluid interfaces and fluid-solid interfaces. While most of these methods were not implemented as part of this work, these descriptions are included here because they were important for the current work.

First, in Section B.1 the stationary modeling of interfaces is discussed. Second, the displacement of the interfaces is discussed in Section B.2. Also, some issues that arose during the implementation of rigid body interaction are described along with the solutions to those issues.

B.1. Interface modeling

This section describes the way interfaces are modeled. As was mentioned in Section 2.1, the VoF-method of Youngs (1984) is used. In § B.1.1 the reconstruction of all interfaces is discussed. Following the generic reconstruction approach, so-called apertures for the solid interface are described in § B.1.2.

B.1.1. Reconstruction

Every time step, the reconstruction of both fraction fields is done using Piecewise Linear Interface Calculation (PLIC). In this approach, the interface in each cell is approximated by a line defined by the equation:

$$m_x x + m_y y = \alpha, \quad (\text{B.1})$$

where m_x and m_y make up the local normal vector and α is the plane constant that places the line at a distance from the cell origin (Duz et al., 2016). For determining the surface normals in each cell, the method by Youngs (1984) is used. The plane constant α in a cell is calculated analytically using the normal vector, cell size and fluid fraction.

B.1.2. Cell apertures

Solid geometries are modelled by using cut-cells that have a volume aperture F_b and surrounding cell face apertures A_x and A_y . A visual depiction is in Figure 2.1b.

For geometries in general, moving or not, the following procedure is used to determine how the cells are cut. The cell face apertures in the presence of a solid body are determined by reconstructing the body surface using the interface reconstruction described previously. The normal vectors and plane constants of the body interface reconstruction are used to calculate the cell face apertures around each

cell where $0 < F_b < 1$.

The above procedure results in two different apertures per cell face (one for each attached cell), which are averaged to find one resulting cell face aperture as in (Fekken, 2004). A correction is applied so that cells with $F_b = 0$ (label B in Figure 2.1a) have a cell face aperture of zero after averaging. These corrected apertures are used for solving the discrete mass and momentum conservation equations.

Several exceptions and additional rules are applied that are needed to fully conserve mass, but they are not considered in the scope of this thesis. For this the reader is referred to (van der Eijk and Wellens, 2021b).

B.2. Interface displacement

The previous Section B.1 described the static representation on an interface, and this section will continue by describing its displacement. First, the displacement of the fluid-fluid (aerated water-air) interface is discussed in § B.2.1, followed by the fluid-solid interface in § B.2.2. An issue that arose during diagonal displacement of solid bodies is described in § B.2.2, along with the solution applied. § B.2.4 describes a technique named virtual cell merging, which helped reduce pressure spikes and was sometimes required for the stable simulation of moving rigid bodies.

B.2.1. Fluid-fluid interface

The transport equation of the VoF function is repeated here from Eq. (2.4):

$$\frac{\partial F}{\partial t} + \mathbf{u} \cdot \nabla F = 0 \quad (\text{B.2})$$

The discrete form that is used in the free surface displacement algorithm is written for the fluid fraction F_s as:

$$F_s^{n+1} = F_s^n - \delta t \nabla \cdot (F_s \mathbf{u})^n = F_s^n - \sum \delta F_s \quad (\text{B.3})$$

The terms δF_s are what we call the VoF mass fluxes defined on the cell faces, which are determined with the COSMIC split scheme to prevent mass loss due to overfluxing (Duz et al., 2016; van der Eijk and Wellens, 2021a). The solid body fluxes and fraction field from the previous time step are used to make sure that $F_s^{n+1} = F_s^{n+1}/F_b^n \leq 1$.

In the transport equation for the free surface, we neglect the compressible term that is described in (van der Eijk, 2018; van der Eijk and Wellens, 2021a). This means that we assume that the fluid volume change due to compressibility is negligible. The effect of this has not been investigated in this thesis. See (van der Eijk, 2018, Section 5.4.2) for a more thorough explanation of these terms.

B.2.2. Fluid-solid interface

The discrete transport equation of the VoF function for the solid body is written here as:

$$F_b^{n+1} = F_b^n - \delta t \nabla \cdot (F_b \mathbf{u})^n = F_b^n - \sum \delta F_b \quad (\text{B.4})$$

Since the solid body is modeled as a nondeformable and incompressible body of fluid, this transport equation is valid. In the original method, the mass fluxes F_b were determined by an unsplit scheme. During diagonal motion of the solid body, the unsplit scheme caused changes in total mass. As a part of this work, the implementation of the COSMIC scheme was used to displace the solid body to prevent this.

B.2.3. Labelling of internal body cells

Even though mass of solid bodies was now exactly conserved during diagonal motion over a straight line, still some issues persisted. During the simulations of pendulum motion in Chapter 5, it was observed that internal body cells may end up with fractions $F_b > 0$ due to the displacement scheme. Body mass was exactly conserved, but the diffusion of body fractions resulted in incorrect cell labelling. Internal body cells that were supposed to have the label B as in figure Figure 2.1a now received the label F or E. The incorrect labels caused the fluid equations to be solved in cells where they should not be solved, sometimes causing the method to crash.

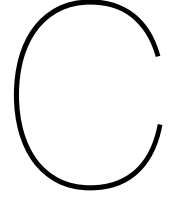
The adopted solution is a new rule for the labeling of B cells based on the fractions F_b in the surrounding 3x3 grid of cells. If the sum of the body fractions $1 - F_b$ in this 3x3 grid is 9 minus a very small error margin, this means that is very likely an internal body cell and should receive the label B. Using this new rule resulted in smooth simulation of pendulum motion in arbitrary direction.

B.2.4. Virtual cell merging

During a simulation with a moving rigid body, it can occur that a computational cell is almost completely filled by solid body. When this happens, the fluid equations are solved over a very small fluid control volume. Due to different time levels of the control volume size in Eq. (2.20), an amplification of the pressure can occur in that cell.

In a simulation where water is assumed incompressible, such pressure spikes vanish quickly. While in a compressible fluid simulation such spikes caused propagating pressure waves contaminating the results. It was also believed to sometimes cause instabilities where the time step became infinitely small due to the CFL controller, however this was not investigated.

The adopted solution was a technique named virtual cell merging. For any cell where $F_b < 0.01$, called child cell, a neighbouring open cell is selected that is called the mother cell. The contributions of the right hand side terms of the Poisson equation for both cells are added to the row of the mother cell. This way, the pressure is solved in a larger control volume and a pressure spike can be prevented.



Material derivative of the density

The conservation of mass can be written for each of the three fluids individually as:

$$\frac{1-F}{\rho_a} \frac{D\rho_a}{Dt} - \frac{DF}{Dt} + (1-F) \nabla \cdot \mathbf{u} = 0 \quad (\text{C.1})$$

$$\frac{\beta F}{\rho_a} \frac{D\rho_a}{Dt} + \beta \frac{DF}{Dt} + F \frac{D\beta}{Dt} + \beta F \nabla \cdot \mathbf{u} = 0 \quad (\text{C.2})$$

$$\frac{(1-\beta)F}{\rho_l} \frac{D\rho_l}{Dt} + (1-\beta) \frac{DF}{Dt} - F \frac{D\beta}{Dt} + (1-\beta) F \nabla \cdot \mathbf{u} = 0 \quad (\text{C.3})$$

Summing these individual conservation equations cancels out both DF/Dt and $D\beta/Dt$:

$$\frac{1-F}{\rho_a} \frac{D\rho_a}{Dt} + \frac{\beta F}{\rho_a} \frac{D\rho_a}{Dt} + \frac{(1-\beta)F}{\rho_l} \frac{D\rho_l}{Dt} + \nabla \cdot \mathbf{u} = 0. \quad (\text{C.4})$$

When assuming isentropic flow (no heat transfer), the acoustic equation of state for density and pressure differences is written as:

$$\frac{Dp}{Dt} = c_l^2 \frac{D\rho_l}{Dt} = c_a^2 \frac{D\rho_a}{Dt}, \quad (\text{C.5})$$

Here c_l and c_a are the speed of sound for liquid water and air, respectively. Using this equation of state, Eq. (C.4) can be simplified to an equation for the material derivative of the pressure:

$$\left(\frac{1-B}{\rho_a c_a^2} + \frac{B}{\rho_l c_l^2} \right) \frac{Dp}{Dt} + \nabla \cdot \mathbf{u} = 0. \quad (\text{C.6})$$

Here $B = (1-\beta)F$ is the amount of liquid in the available space in the control volume. The material derivatives of F and β can be found by isolating Dp/Dt from Eq. (C.6):

$$\frac{Dp}{Dt} = - \frac{\rho_a c_a^2 \rho_l c_l^2}{(1-B) \rho_l c_l^2 + B \rho_a c_a^2} \nabla \cdot \mathbf{u} \quad (\text{C.7})$$

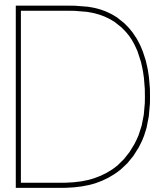
Substituting this into Eq. (C.1) for mass conservation of air above the free surface results in the material derivative of F :

$$\frac{DF}{Dt} = (1-F) H \nabla \cdot \mathbf{u} \quad \text{with} \quad H = \frac{B(\rho_a c_a^2 - \rho_l c_l^2)}{(1-B) \rho_l c_l^2 + B \rho_a c_a^2}. \quad (\text{C.8})$$

The material derivative of β is obtained by substituting Eq. (C.7) and Eq. (C.8) into the mass conservation of air inside the homogeneous mixture:

$$\frac{D\beta}{Dt} = -\beta \frac{F_b}{F_s} H \nabla \cdot \mathbf{u} \quad (\text{C.9})$$

All terms needed to find an expression for $D\rho/Dt$ are now available.



Additions to the numerical method

This appendix chapter contains a complete overview of features added to the method in the duration of this graduation project. First, a list is presented with corresponding references to where they were introduced in this thesis. If they were not introduced in the body of this thesis, they are included in the sections of this chapter

- A new version of the poisson equation solver that strongly couples the body motion to the fluid in a monolithic way in Section 2.4.
- An additional extension of the monolithic solver for pendulum motion in Section 5.1.
- Calculatons for three different analytical wave theories in Section 3.1.
- The implementation of wave inflow conditions in Section 3.2.
- The implementation of periodic boundary conditions in Section 3.3.
- A geometry module for approximating initial fraction fields using signed distance functions Section D.1.
- Methods for geometrical grid spacing in Section D.2.

D.1. Arbitrary fraction field initialisation

Signed distance functions can be used to define simple geometric primitives. A signed distance function represents the shortest distance (negative when inside the body) to the body surface from the point of evaluation. Simple primitives can be combined using regularized Boolean set operators to form arbitrarily shaped bodies. This process is called constructive solid geometry (CSG), which is used in many CAD applications.

Using CSG, points on a grid can be evaluated to see whether they are inside or outside the defined solid. By evaluating multiple points in a grid cell, an approximation can be found of the solid volume inside that grid cell. This process is similar to a Marker-and-Cell method as described by Kleefsman (2005). The actual reconstruction of the body surface on the grid is only based on the body fractions. Some detail is lost with respect to the CSG body definition, but this is the limit of the surface reconstruction techniques used.

An example of where this is already applied in the current project is in the shape of the "wedge-block". While this shape is still simple and an analytic and parametric fraction field could be determined relatively easy, the Boolean union operator made this shape a simple combination of a rectangle and a triangle whose primitive signed distance functions were already available.

The above is only used at the initialization of the simulation, because the body fractions are displaced using the same algorithm as the fluid displacement to conserve mass. The translation and rotation of a CSG object is very straightforward, so it could be time-integrated together with the body fluxes to use as a measure of detail loss over travel distance. As most of the simulations done in the current phase of this study use only uni-directional translations, this has not been done yet.

D.2. Stretching grid cells

Two methods for creating structured non-uniform grids are implemented. Both are implemented using NumPy functions (Harris et al., 2020). The first method (Simple) is defined by a ratio between the center cell and the outer cell along a dimension. The second method (Detail) allows input in the form of uniform interior bands with stretching towards the edges of the domain.

D.2.1. Simple

Using a ratio between the size of the outermost cell and the innermost cell (center) of the numerical domain, a grid can be created where the cell size increases with a geometrical progression. This means that subsequent cell sizes increase with a constant ratio r . The method is explained in one dimension, but can be applied in two directions. The input for an axis consists of domain length L , the total number of cells N and the ratio R between the outer and inner cells. From this input, the following types of grids are created:

- Uniformly spaced grids by setting $R = 1$
- Non-uniformly spaced grids
 - with smaller cells in the center by setting $R > 1$
 - with smaller cells around the edges by setting $R < 1$

First, a sequence Δx of length M is generated using `np.geomspace`. Here M is found from a floor division of the total number of cells N :

$$M = \left\lfloor \frac{N + 1}{2} \right\rfloor.$$

Then Δx_n for $n = 0, 1, \dots, M - 1$ is defined as:

$$\Delta x_n = \left({}^{(M-1)}\sqrt{R} \right)^n.$$

This is a sequence from 1 to R with a geometric progression ratio $r = {}^{M-1}\sqrt{R}$.

For an even amount of total cells N , the length M simply evaluates to $N/2$. The geometric sequence is then doubled by mirroring it around the first entry $\Delta x_0 = 1$. The result is a sequence of length N with values $\Delta x_0 = R$, $\Delta x_{M-1} = 1$, $\Delta x_M = 1$ and $\Delta x_N = R$.

For an uneven amount of total cells N , the length M is larger than $N/2$. The geometric sequence is doubled similarly as for an even amount of cells, but one of the two $\Delta x = 1$ entries is left out. The result is a sequence of length N with values $\Delta x_0 = R$, $\Delta x_{M-1} = 1$ and $\Delta x_N = R$.

The sum of the sequence Δx is an arbitrary value, so all elements in the sequence are multiplied by $L / \sum \Delta x$ to obtain the final grid spacing as used in the simulation.

D.2.2. Detail

For situations where the region of interest is not necessarily in the center of the domain, a more detailed input can be provided. Similar to the previous method, the current is explained in one dimension, but can be applied in two directions. The input for an axis consists of domain length L , a bounded region

$[X_L, X_R]$ and the amount of same-size cells N inside this banded region. Additionally, two maximum progression ratios $[r_{L,\max}, r_{R,\max}]$ are defined for both outer sides of the bounded region.

The procedure at one side of the bounded region is described here. Consider this the right side of the bounded region with length $L_R = L - X_R$. Given the maximum ratio, the number of cells M needed to fill length L_R is found from the condition:

$$\Delta x_c \cdot \sum_{k=1}^M r_{R,\max}^k \geq L_R, \quad (\text{D.1})$$

where Δx_c is the constant cell size inside the bounded region. To determine the actual ratio r_R that will fit M cells exactly in length L_R , the following polynomial is solved using `np.roots`:

$$\Delta x_c \cdot \sum_{k=1}^M r_R^k = L_R.$$

With this ratio, the geometric sequence $\Delta x_{R,n}$ is defined for $n = 0, 1, \dots, M - 1$ as:

$$\Delta x_{R,n} = \Delta x_c \cdot r_R^{1+n}$$

By repeating this procedure for the other side, a cell spacing can be defined with a constant band and different geometric progressions to both sides of the domain.

The above can be used with ratios $r < 1$, but then this is considered the minimum ratio between subsequent cells. The same procedure is followed, but $M - 1$ is taken from the result of Eq. (D.1) to enforce the chosen r as a minimum ratio. Care has to be taken that this ratio is not taken too small for length L_R that has to be covered, otherwise Eq. (D.1) has no solution. The code will give an error if this happens.

Initial periodic wave comparison

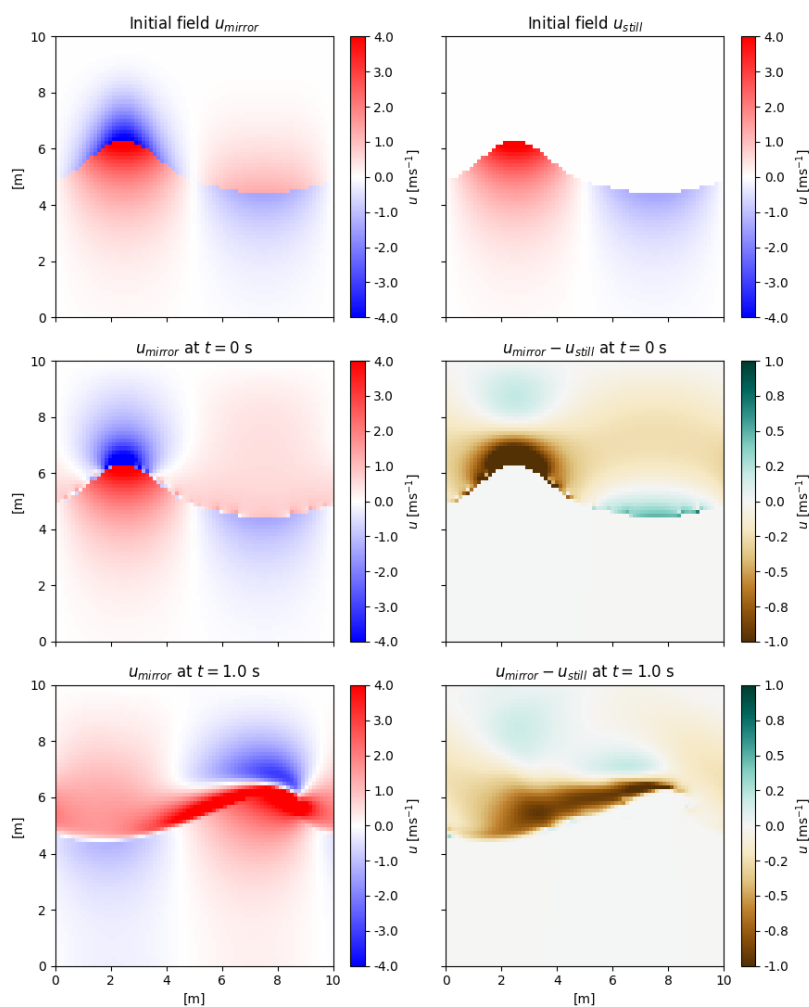


Figure E.1: Comparison between wave with and without extrapolating initial air velocities. It shows no observable differences in the fluid velocities.

F

Focused steep wave

Period [s]	Height [m]	Phase [rad]
3.997400	0.001103	-0.627860
3.331167	0.002849	+2.074318
2.855286	0.000958	-2.091860
2.498375	0.007391	+2.629218
2.220778	0.015701	-1.261249
1.998700	0.023661	+1.762357
1.817000	0.033372	-1.250876
1.665583	0.033822	+2.253255
1.537462	0.017892	-1.227521
1.427643	0.028456	+1.630720
1.332467	0.014018	-1.631556
1.249187	0.019171	+0.772899
1.175706	0.009490	-2.767128
1.110389	0.014243	-0.472141
1.051947	0.008088	+1.852184
0.999350	0.011541	-1.987130
0.951762	0.008885	+0.240174
0.908500	0.008217	+2.901381
0.869000	0.005392	-1.372552
0.832792	0.004651	+0.116720
0.799480	0.005138	+1.464443

Table F.1: Wave parameters for focused wave in Chapter 5.

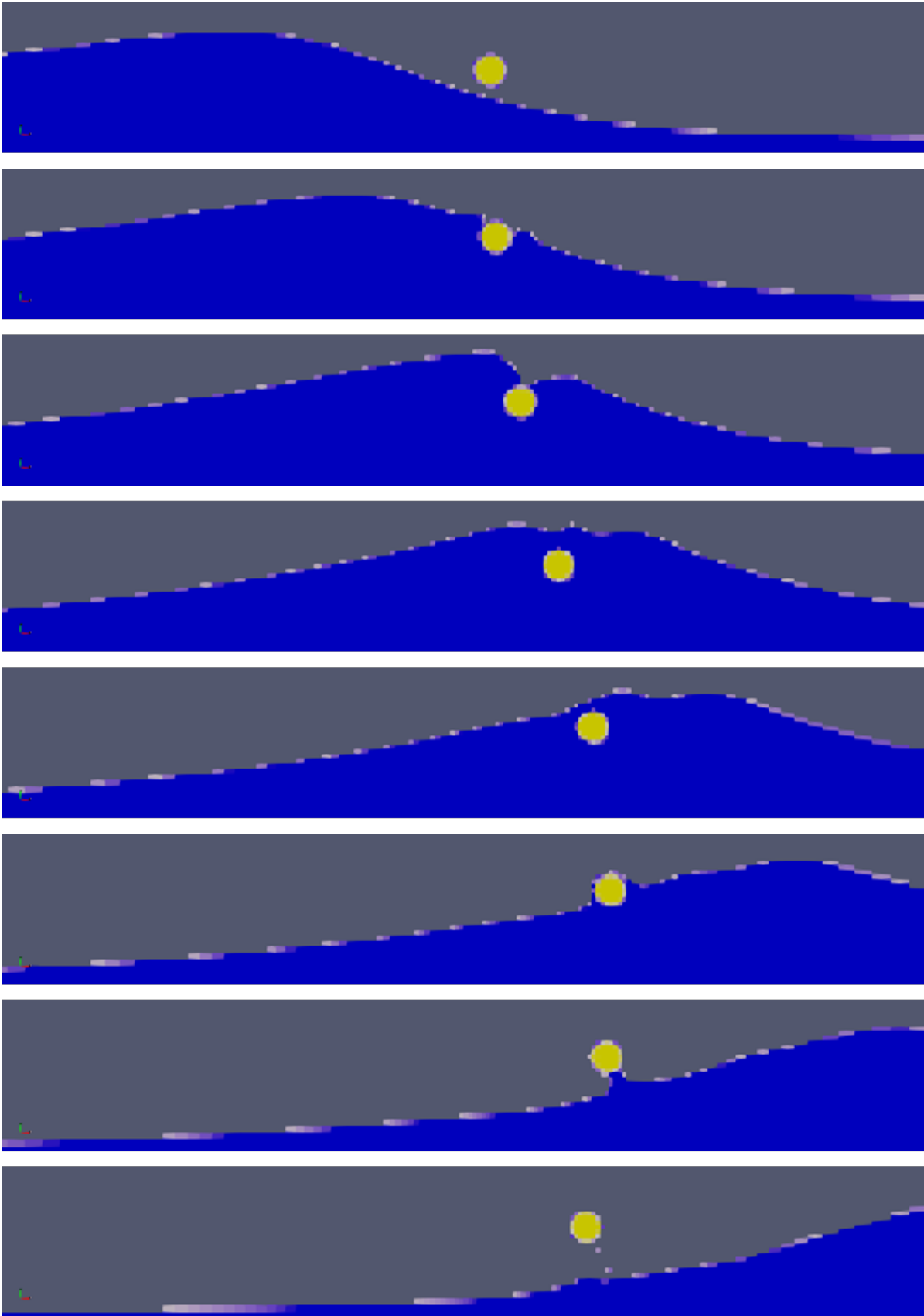


Figure F.1: Snapshots of the steep wave impact on the pendulum.